Friction

Research Article

Mixed and thermal elastohydrodynamic simulation of a low-loss gear considering the gear system

Felix Farrenkopf✉, Thomas Lohner, Karsten Stahl

Cite this article: Farrenkopf F, Lohner T, Stahl K. *Friction* 2025, **13**(10): 9441096. https://doi.org/10.26599/FRICT.2025.9441096

ABSTRACT: The reduction of load-dependent gear power loss is one of the key aspects in gear design. Therefore, a detailed power loss prediction and the local investigation of its drivers are essential. In this study, the model of Farrenkopf et al. is stepwise enhanced to match the real contact conditions as closely as possible. The impact of eliminating simplifications or assumptions is shown at each of the individual enhancement steps. The proper choice of the lubricant parameters, the coefficient of solid friction, and the gear system stiffness shows a great impact on load-dependent gear power losses and the local friction. It is explained how the load-dependent gear power loss of an individual tooth contact is derived from the transient local TEHL contact and subsequently the measurable load-dependent gear power loss. Considering a low-loss gear geometry, the simulation results are compared with experimental results and show a good level of conformity.

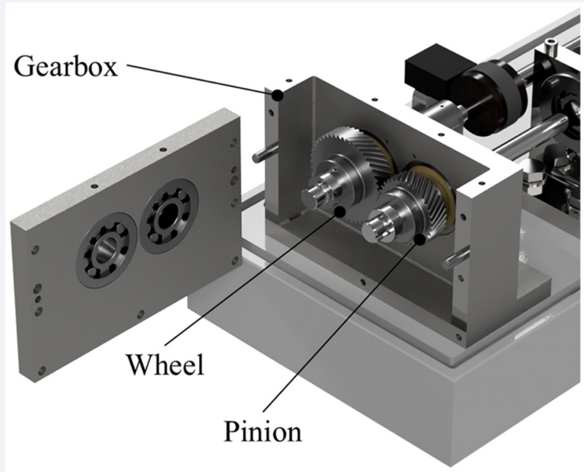

KEYWORDS: elastohydrodynamic lubrication; mixed lubrication; gear; efficiency

1 Introduction

The challenges posed by climate change have increased awareness of efficiency, sustainability, and life cycle analysis, not only in the engineering sector but in society as a whole. When designing gears, various technologies are employed to reduce load-dependent gear power losses, such as the use of coatings [1], modification of surface topographies [2, 3], low-viscosity lubricants [4], or adaption of geometries by the use of so-called low-loss geometries [2]. To fully benefit from these potentials, it is essential to conduct a detailed power loss calculation and a local investigation of the lubricated gear contact.

The total power loss of a gearbox P_{L} is the sum of the component power losses of the gears (index G), bearings (index B), seals (index S), and other components (index X) [5]. The load-dependent portions occur in the rolling-sliding contacts under load (index P), whereas the no-load losses are driven by gearbox fluid flow (index 0):

$$P_{\mathrm{L}} = P_{\mathrm{LG0}} + P_{\mathrm{LGP}} + P_{\mathrm{LB0}} + P_{\mathrm{LBP}} + P_{\mathrm{LS}} + P_{\mathrm{LX}} \tag{1}$$

The relative power loss ζ is defined as the ratio between the power losse P_{L} and input power P_{in}:

$$\zeta = \frac{P_{\mathrm{L}}}{P_{\mathrm{in}}} = \frac{P_{\mathrm{in}} - P_{\mathrm{out}}}{P_{\mathrm{in}}} = 1 - \eta \tag{2}$$

The efficiency η is the complement of ζ. The load-dependent gear power losses are defined by

$$P_{\mathrm{LGP}} = \frac{1}{p_{\mathrm{et}}} \cdot \int_{\bar{y}=0}^{b} \int_{\bar{x}=\mathrm{A}}^{E} f_{\mathrm{N}}(\bar{x},\bar{y}) \cdot \mu(\bar{x},\bar{y}) \cdot v_{\mathrm{g}}(\bar{x},\bar{y})\, \mathrm{d}\bar{x}\mathrm{d}\bar{y} \tag{3}$$

Several calculation methods can be classified as mesh-averaged or mesh-local. Mesh-local methods can be further distinguished as contact-averaged and contact-local methods.

The mesh-averaged approaches are among the simplest methods for calculating load-dependent gear power losses. These approaches assume a mean coefficient of gear friction μ_{mz}. Using this assumption, Eq. (3) can be rewritten as

$$P_{\mathrm{LGP}} = P_{\mathrm{in}} \cdot \mu_{\mathrm{mz}} \cdot \underbrace{\frac{1}{p_{\mathrm{et}}} \cdot \int_{\bar{y}=0}^{\mathrm{b}} \int_{\bar{x}=\mathrm{A}}^{\mathrm{E}} \frac{f_{\mathrm{N}}(\bar{x},\bar{y})}{F_{\mathrm{bt}}} \cdot \frac{v_{\mathrm{g}}(\bar{x},\bar{y})}{v_{\mathrm{tb}}} \mathrm{d}\bar{x}\mathrm{d}\bar{y}}_{=H_{\mathrm{VL}}} \tag{4}$$

Ohlendorf [6], Michaelis [7], Schlenk [8], and Doleschel [9] provided approaches to calculate the mean coefficient of gear friction μ_{mz}. Ohlendorf [6] and Wimmer [10] proposed an

Gear Research Center (FZG), Department of Mechanical Engineering, School of Engineering and Design, Technical University of Munich, Boltzmannstraße 15, D-85748 Garching near Munich, Germany.

✉ Corresponding author. E-mail: felix.farrenkopf@tum.de

Received: May 2, 2024; Revised: November 14, 2024; Accepted: March 18, 2025

Nomenclature

Symbol

A	First point of contact on path of contact (−)
a	Center distance (m)
b	(Common) face width (m)
C	Pitch point (−)
c_p	Specific heat capacity (J/(kg·K))
corr	Tooth flank geometry modification (m)
E	Last point of contact on path of contact (−)
$E_{1;2;\mathrm{eq}}$	Young's modulus (N/m²)
F_{bt}	Load at base circle (N)
F_{N}	Normal load (N)
f_{N}	Line load (N/m)
f_{z}	Gear mesh frequency (1/s)
h	Lubricant film thickness (m)
h_0	Rigid body separation (m)
h_{c}	Central film thickness (m)
h_{def}	Accumulated deformation (m)
h_{m}	Minimum film thickness (m)
$H_{\mathrm{V(L)}}$	(Local geometric) tooth power loss factor (−)
k	Coefficient of thermal distribution (−)
m_{n}	Normal module (m)
P	Power (W)
P'	Linear power density (W/m)
p	Pressure (N/m²)
p_{et}	Transverse base pitch (m)
$\dot{q}$	Heat flux density (W/m²)
R_{red}	Reduced radius of curvature (m)
t	Time (s)
t_{c}	Time of a single contact line during its transition through the tooth flank contact area (s)
T	Temperature (K)
$T_{1;2}$	Torque (1 = pinion, 2 = wheel) (N·m)
v	Velocity/speed (m/s)
$v_{\mathrm{t,C}}$	Circumferential speed (pitch point) (m/s)
v_{t}	Tangential velocity (m/s)
v_{tb}	Tangential speed at base diameter (m/s)
X, Y, Z	Dimensionless EHL coordinate system (−)
x, y, z	EHL coordinate system (m)
$\bar{x}, \bar{y}$	Coordinate system of tooth flank contact area (m)
$z_{1;2}$	Number of teeth (−)

Greek symbol

α_{n}	Pressure angle (°)
β	Helix angle (°)
$\dot{\gamma}$	Shear rate (1/s)
δ	Elastic deformation (m)
η	Dyn. viscosity (Pa·s)
λ	Thermal conductivity (W/(m·K))
μ	Coefficient of friction (−)
$\nu_{1;2;\mathrm{eq}}$	Poisson coefficient (−)
ζ	Relative power loss (%)
ρ	Density (kg/m³)
σ	Stress tensor (N/m²)
τ	Shear stress (N/m²)
τ_{C}	Eyring shear stress (N/m²)
$\Phi^{\mathrm{p;s}}$	Pressure/shear flow factor (−; m)
ψ	Power density = P'' (W/m²)
Ω	Calculation domain (m²)

Indice

0	No-load/initial
1, 2	Body 1, body 2
B	Bearing
δ	Elastic deformation
eq	Equivalent
exp	Experimental
ext	Extended
f	Fluid
G	Gear
g	Sliding
in	Input
L	Loss
M	Bulk
m	Mean
mz	Mean gear
out	Output
P	Load-dependent
p	Pressure
S	Seal
s	Solid
T	Temperature
X	Other components
x, y, z	x-, y-, z-coordinate

analytical approach for the tooth power loss factor H_{V}, while Wimmer [10] introduced a local geometric tooth power loss factor H_{VL}, considering numerical load distribution by a loaded tooth contact analysis (LTCA).

Mesh-local approaches are based on a local coefficient of friction. Mesh-local and contact-averaged approaches usually use approximation methods based on Hertzian theory for the coefficient of friction. In 1961, Benedict and Kelley [11] developed a formula to estimate the coefficient of friction based on viscosity, load, and velocity conditions. Xu et al. [12] proposed a formula for the coefficient of friction resulting from linear regression analysis of an EHL model. Quiban et al. [13], Arana et al. [14], Mayer [15], and Matsumoto and Morikawa [16] estimated the load-sharing of solid contact and hydrodynamics based on the lubricant film thickness equations of Grubin [17], Dowson and Higginson [18], and Hamrock and Dowson [19].

Mesh-local and contact-local approaches involve calculating power losses based on contact-local shear stress. Wang et al. [20] used a TEHL model considering Newtonian fluid behavior and smooth surfaces, while Larsson [21] and Mihailidis and Panagiotidis [22] considered non-Newtonian fluid equations. Ziegltrum et al. [23] and Lohner [24] used an FEM-based TEHL model, with Lohner [24] assuming smooth surfaces and Ziegltrum et al. [23] using the load-sharing approach of Ref. [9]. Instead of an FEM model for the calculation of the elastic contact deformation, half-space approaches are used in Refs. [20–22, 25, 26]. Bobach et al. [26], Beilicke et al. [25], and Farrenkopf et al. [27] are capable of calculating the complete three-dimensional TEHL contact depending on the time t. Despite using FEM or half-space approaches, current models often neglect the deformation of bearings, shafts, the gear body, and the tooth and use further simplified boundary conditions such as cylindrical and equal-length contact bodies and the increased gear bulk temperature in operation.

The different approaches use specific simplifications or assumptions, even when mesh- and contact-local. The author's work in Ref. [27] demonstrates that a mesh- and contact-local approach for power loss calculation can be created using an FEM-based TEHL model. This study builds upon that configuration as a reference and has the objective to incrementally eliminate assumptions and simplifications to enhance the model and match the actual gear contact conditions more closely. The following step-by-step improvements are investigated:

- The deformations of the shafts, bearings, gear body, and gear tooth are considered as they affect the geometry of the contact bodies.
- The roughness and surface topography, including the orientation of grinding marks, are considered as they influence the fluid flow and load-sharing.
- The difference in bulk and oil temperature in stationary operating points is taken into account.
- The coefficient of solid friction is estimated based on experimental results.
- The tooth root stiffness and heat conduction is considered, as it influences contact pressure and temperature.

2 Methods and materials

In this section, the object of investigation is introduced, followed by a description of the loaded tooth contact analysis, the thermal network method, the thermal elastohydrodynamic lubrication model, and the calculation of load-dependent gear power losses.

2.1 Object of investigation

The object of investigation is the test gearbox of an FZG efficiency test rig, as outlined by Hinterstoißer et al. [2] (Fig. 1). Following the approach of Farrenkopf et al. [27], the corresponding moderate low-loss gear is considered, with a module of $m_n = 1.92$ mm, a center distance of $a = 91.5$ mm, a pressure angle of $\alpha_n = 27°$, a helix angle of $\beta = 33°$, $z_1 : z_2 = 34 : 46$ number of teeth, and a lead crowning of $C_\beta = 6.5$ μm. The pinion torque of $T_1 = 208$ N·m and a circumferential speed of $v_{t,C} = \{2, 8.3, 20\}$ m/s are considered with adapted rotational direction. The gearbox is dip-lubricated with an ISO VG 100 mineral oil at 363.15 K. The bearings used are of type NU406-XL-M1, while the gear bulk and shaft materials are considered as case-carburized steel (16MnCr5) with ground and run-in gear flanks. According to Hintersoißer [28], a flank surface roughness of $R_a = 0.19$ μm is taken into account. This setup enables a comparison of the numerically calculated results with experimental results from Hinterstoißer [2].

Bartel [29] described solid friction as the interaction of deformation, adhesion, and tribochemical processes. An approximate value for the coefficient of solid friction can be obtained by measuring power loss or friction under operating conditions with a high solid load portion using the oil and surfaces under consideration. Based on gear test results of Lohner [24] using the identical ISO VG 100 mineral oil at 363.15 K and ground gears, the coefficient of solid friction of the considered oil is estimated as $\mu_s = 0.08$. This value differs from Ref. [27], in which $\mu_s = 0.05$ was used, based on Bobach et al. [1].

2.2 Loaded tooth contact analysis

The software RIKOR [30] is used to perform the LTCA. It is a multi-body system for calculating the deformation of gears, shafts, and bearings. To do this, a system of individual stiffnesses is assembled and solved. Unlike the previous work by Farrenkopf et al. [27], the bearings and shafts are not modeled rigidly to evaluate the influence of their stiffness and deformation. Therefore, the software RIKOR was adapted to allow access to the needed values instead of converting the standard output. Note that extended tooth contact and meshing effects are not considered in the conducted LTCA. Their effects are expected to be small for the gear geometries and loads considered.

Figure 2 shows the results of the LTCA. The reduced radius of curvature $R_{red}(\bar{x})$ and the tooth flank geometry modification $\mathrm{corr}(\bar{y})$, defining the undeformed tooth geometry of the considered moderate low-loss gear, are presented in Figs. 2(a) and 2(b). The tooth flank geometry modification $\mathrm{corr}(\bar{y})$ due to the lead corwning is understood as an intended geometric modification of the tooth flank geometry compared to the (involute) main gear geometry (DIN ISO 21771 [31]). The normal force $F_N(t)$ is given for $v_{t,C} = \{2, 8.3, 20\}$ m/s in Fig. 2(c). $R_{red}(\bar{x})$, $v_g(\bar{x})$, and $v_m(\bar{x})$ remain constant along the tooth width $\bar{y}$, while $\mathrm{corr}(\bar{y})$ is constant along the line of action $\bar{x}$. The total contact time t_c decreases with increasing circumferential speed. The sliding velocity $v_g(\bar{x}) = v_2(\bar{x}) - v_1(\bar{x})$, and mean velocity $v_m(\bar{x}) = (v_1(\bar{x}) + v_2(\bar{x}))/2$ are shown in Figs. 2(d) and 2(e). All

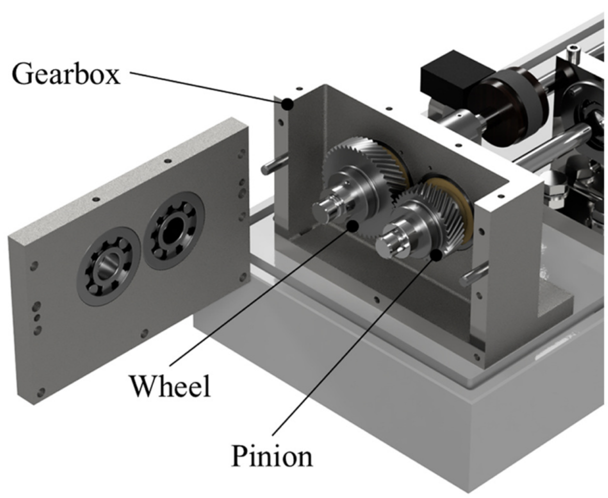

Fig. 1 Test gear box of a FZG efficiency test rig with low-loss gear.

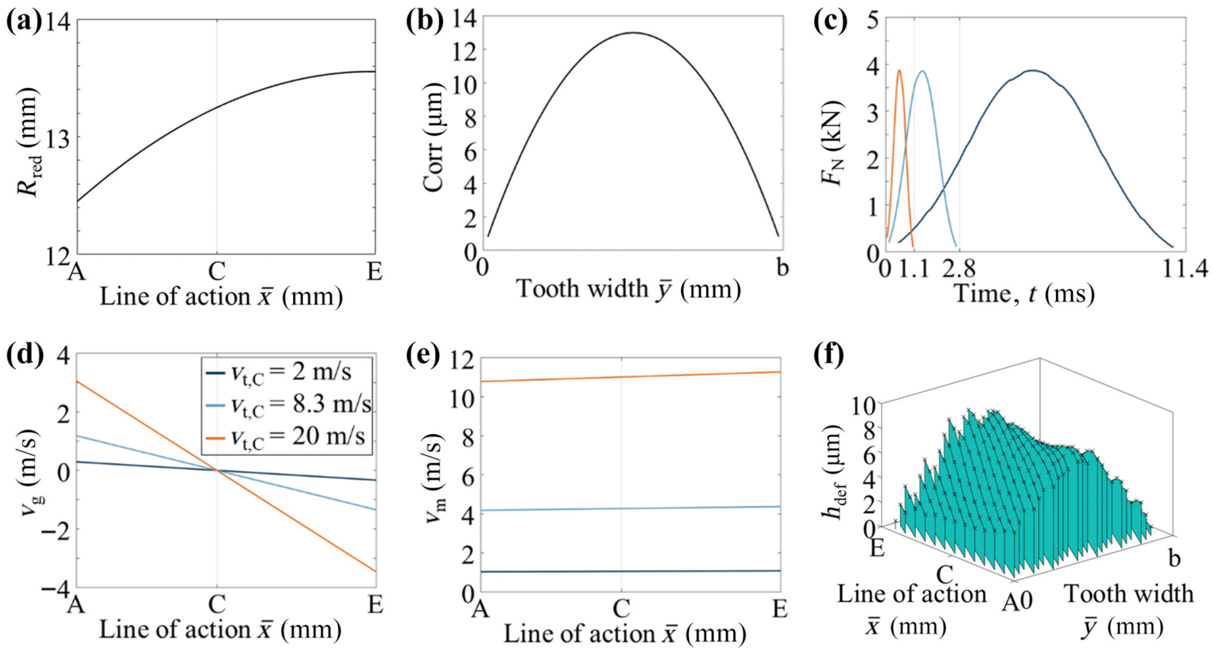

Fig. 2 (a) Reduced radius $R_{red}(\bar{x})$, (b) tooth flank geometry modification $\mathrm{Corr}(\bar{y})$, (c) normal force $F_N(t)$, (d) sliding velocity $v_g(\bar{x})$, (e) mean velocity $v_m(\bar{x})$, and (f) accumulated deformation $h_{def}(\bar{x},\bar{y})$.

relevant deformations of the gear system that are calculated in the LTCA, including the bearing, shaft, gear body, and tooth deformations, are summed up in the accumulated deformation $h_{def}(y,t)$. Hertzian contact deformations are excluded in the LTCA since elastic contact deformation is calculated in the mixed TEHL model. Also, housing deformations are not considered. Figure 2(f) shows the accumulated deformation $h_{def}(y,t)$ for $v_{t,C}=8.3$ m/s. Since the tooth tip and tooth root are meshing according to the contact ratios of the moderate low-loss gear, a mean stiffness is prevailing for the system. The symmetrical shaft bearing of the gears results in a symmetrical accumulated deformation in tooth width direction with decreasing value to the gear faces.

Please note the usage of different coordinate systems: $(\bar{x},\bar{y})$ for the tooth flank contact area and (x,y,z) for the TEHL simulation. For more detailed information, the reader is referred to Ref. [27].

2.3 Thermal network method

Since lubricant properties such as viscosity $\eta(T,p)$, the density $\rho(T,p)$, and the specific heat capacity $c_p(T,p)$ are strongly influenced by temperature distribution, the most accurate estimate of the gear bulk temperature T_M is important. To achieve this, a thermal network method (TNM) was used. This method treats thermal conductivities as electrical resistors in a thermal Ohm's law. The model of Paschold et al. [32] for the FZG efficiency test rig is used, substituting the gear geometry and using the measured load-dependent gear power losses of Hinterstoißer [2]. For $T_1 = 208$ N·m, $v_{t,C}=\{2, 8.3, 20\}$ m/s, and $T_{oil}=363.15$ K, gear bulk temperature of $T_M=\{364.7, 366.1, 367.4\}$ K are calculated. The comparable small increase of T_M is related to the considered low-loss gear geometery.

2.4 Mixed thermal elastohydrodynamic lubrication model

The considered mixed TEHL model is based on the author's previous work [27]. To achieve reasonable calculation times for mixed lubrication, it is based on the indirect coupling of micro and macro hydrodynamics using flow factors and integral solid pressure curves. Therefore, this section provides a condensed overview that focuses on the differences. These differences include an extension of the lubricant film thickness equation and changes to the calculation domains, which affect the structural mechanics and energy equation. The following subsections describe the governing equations, the calculation domains, the mixed lubrication, the lubricant equations, and the numerical procedure.

2.4.1 Governing equations

As governing equations, the generalized Reynolds equation, the calculation of the lubricating film thickness, the structural mechanics, the calculation of the lubricant velocities, shear rates, and shear stresses, the balance of forces, and the thermal energy equation are described below.

The lubricant film thickness $h(x,y,t)$ in Eq. (5) is determined by the geometry of the contact bodies, the rigid body separation $h_0(t)$, and the elastic contact deformation $\delta(x,y,t)$ of the contact bodies. The contact geometry of the gear tooth contact is described by the substitution body approach with a reduced radius $R_{red}(y,t)$, that varies in time and along the contact line. The tooth flank geometry modification $\mathrm{corr}(y,t)$ can also be described along the contact line and in time. The accumulated deformation $h_{def}(y,t)$ is considered as quantified by the LTCA (Section 2.2). Using an equivalent system of contact bodies, like in previous work [27] (standard EHL calculation domain), the elastic deformation of both contact bodies is combined in $\delta_{1,2}(x,y,t)$. Using two separated contact bodies (extended EHL calculation domain), the elastic deformation is composed of $\delta_{1,2}(x,y,t)=\delta_1(x,y,t)+\delta_2(x,y,t)$.

$$h(x,y,t)=h_0(t)+\underbrace{\frac{x^2}{2R_{red}(y,t)}+\mathrm{corr}(y,t)+h_{def}(y,t)}_{\text{Gear geometry}}+\delta_{1,2}(x,y,t) \tag{5}$$

In all cases, the elastic contact deformation $\delta(x,y,t)$ can be calculated by the structural mechanics

$$\nabla \cdot \sigma = 0 \tag{6}$$

When using the equivalent system of the standard EHL calculation domain, it is necessary to use the equivalent material properties of Habchi [33] (E_{eq} and ν_{eq}). If the extended EHL calculation domain is used, the individual material properties must be used ($E_{1;2}$ and $\nu_{1;2}$).

The generalized Reynolds equation in Eq. (7) is used to describe the fluid flow. The formulation of Habchi [33], which includes thermal and non-Newtonian effects, is employed along with the extensions of the flow factors $\Phi^{\mathrm{p;s}}_{xx;yy}(h)$, according to Bartel [29]. The definition of Bartel [29] extends the approach of Patir and Cheng [34, 35] for non-Newtonian fluid behavior.

$$\frac{\partial}{\mathrm{d}x}\left(\Phi^{\mathrm{p}}_{xx}\varepsilon\frac{\partial p_{\mathrm{f}}}{\partial x}\right)+\frac{\partial}{\mathrm{d}y}\left(\Phi^{\mathrm{p}}_{yy}\varepsilon\frac{\partial p_{\mathrm{f}}}{\partial y}\right)=\frac{\partial \rho_x^*}{\partial x}+\frac{\partial \rho_y^*}{\partial y}+\frac{\partial \rho_{\mathrm{e}}}{\partial t} + \frac{\partial}{\partial x}\left(\rho_{\mathrm{e}}\frac{(v_{2,x}-v_{1,x})}{2h}\Phi^{\mathrm{s}}_{xx}\right)+\frac{\partial}{\partial y}\left(\rho_{\mathrm{e}}\frac{(v_{2,y}-v_{1,y})}{2h}\Phi^{\mathrm{s}}_{yy}\right) \tag{7}$$

with $\varepsilon = \frac{\eta_{\mathrm{e}}}{\eta_{\mathrm{e}}'}\rho' - \rho''$ and $\rho' = \int_0^h \rho \int_0^z \frac{\mathrm{d}z'}{\eta}\mathrm{d}z$ and $\rho'' = \int_0^h \rho \int_0^z \frac{z'\mathrm{d}z'}{\eta}\mathrm{d}z$ and $\rho_x^* = \rho_{\mathrm{e}} v_{1,x} + \eta_{\mathrm{e}}(v_{2,x}-v_{1,x})\rho'$ and $\rho_y^* = \rho_{\mathrm{e}} v_{1y} + \eta_{\mathrm{e}}(v_{2,y}-v_{1,y})\rho'$ and $\frac{1}{\eta_{\mathrm{e}}} = \int_0^h \frac{\mathrm{d}z}{\eta}$ and $\frac{1}{\eta_{\mathrm{e}}'} = \int_0^h \frac{z}{\eta}\mathrm{d}z$ and $\rho_{\mathrm{e}} = \int_0^h \rho \mathrm{d}z$

Habchi [33] provided the equations that define the velocities within the lubricant

$$\begin{aligned} v_{\mathrm{f},x} &= \frac{\partial p_{\mathrm{f}}}{\partial x}\left(\int_0^z \frac{z'}{\eta}\mathrm{d}z' - \frac{\eta_{\mathrm{e}}}{\eta_{\mathrm{e}}'}\int_0^z \frac{1}{\eta}\mathrm{d}z'\right) + \eta_{\mathrm{e}}(v_{2,x}-v_{1,x})\int_0^z \frac{1}{\eta}\mathrm{d}z + v_{1,x} \\ v_{\mathrm{f},y} &= \frac{\partial p_{\mathrm{f}}}{\partial y}\left(\int_0^z \frac{z'}{\eta}\mathrm{d}z' - \frac{\eta_{\mathrm{e}}}{\eta_{\mathrm{e}}'}\int_0^z \frac{1}{\eta}\mathrm{d}z'\right) + \eta_{\mathrm{e}}(v_{2,y}-v_{1,y})\int_0^z \frac{1}{\eta}\mathrm{d}z + v_{1,y} \end{aligned} \tag{8}$$

as well as the shear rates

$$\begin{aligned} \dot{\gamma}_{zx} &= \frac{1}{\eta}\frac{\partial p_{\mathrm{f}}}{\partial x}\left(z - \frac{\eta_{\mathrm{e}}}{\eta_{\mathrm{e}}'}\right) + \frac{\eta_{\mathrm{e}}}{\eta}(v_{2,x}-v_{1,x}) \\ \dot{\gamma}_{zy} &= \frac{1}{\eta}\frac{\partial p_{\mathrm{f}}}{\partial y}\left(z - \frac{\eta_{\mathrm{e}}}{\eta_{\mathrm{e}}'}\right) + \frac{\eta_{\mathrm{e}}}{\eta}(v_{2,y}-v_{1,y}) \end{aligned} \tag{9}$$

The hydrodynamic shear stress τ_{f} can be evaluated by

$$\tau_{\mathrm{f}} = \sqrt{\tau_{\mathrm{f},zx}^2 + \tau_{\mathrm{f},zy}^2} \tag{10}$$

with the directional components calculated as Eq. (11):

$$\begin{aligned} &\tau_{\mathrm{f},zx} = z\frac{\partial p_{\mathrm{f}}}{\partial x} + \tau_{zx}^0 \text{ with } \tau_{zx}^0 = \tau_{\mathrm{f},zx}(z=0) \text{ and} \\ &\int_{z_1}^{z_2} \frac{z\frac{\partial p}{\partial x} + \tau_{zx}^0}{\eta}\mathrm{d}z = v_{2,x} - v_{1,x} \\ &\tau_{\mathrm{f},zy} = z\frac{\partial p_{\mathrm{f}}}{\partial y} + \tau_{zy}^0 \text{ with } \tau_{zy}^0 = \tau_{\mathrm{f},zy}(z=0) \text{ and} \\ &\int_{z_1}^{z_2} \frac{z\frac{\partial p}{\partial y} + \tau_{zy}^0}{\eta}\mathrm{d}z = v_{2,y} - v_{1,y} \end{aligned} \tag{11}$$

The coefficient of fluid friction μ_{f} is calculated by integrating the shear stress $\tau_{\mathrm{f},zx}$ along the contact domain Ω_{p}, evaluated in the middle of the lubricant film thickness at $z = h/2$:

$$\mu_{\mathrm{f}} = \frac{\int_{\Omega_{\mathrm{p}}} \tau_{\mathrm{f},zx}|_{z=h/2}\mathrm{d}\Omega_{\mathrm{p}}}{F_{\mathrm{N}}} \tag{12}$$

The balance of forces must be ensured. To achieve this, the applied normal force F_{N} must be equal in size to the resulting force from hydrodynamic pressure p_{f} and solid contact pressure p_{s}:

$$F_{\mathrm{N}}(t) - \int_{\Omega_{\mathrm{p}}} p_{\mathrm{f}}(x,y,t)\,\mathrm{d}\Omega_{\mathrm{p}} - \int_{\Omega_{\mathrm{p}}} p_{\mathrm{s}}(x,y,t)\,\mathrm{d}\Omega_{\mathrm{p}} = 0 \tag{13}$$

The temperature distribution is calculated using the energy equation for the lubricant:

$$\begin{aligned} &\frac{\partial}{\partial x}\left(\lambda\frac{\partial T}{\partial x}\right)+\frac{\partial}{\partial y}\left(\lambda\frac{\partial T}{\partial y}\right)+\frac{\partial}{\partial z}\left(\lambda\frac{\partial T}{\partial z}\right) \\ &-\rho c_p\left(v_{\mathrm{f},x}\frac{\partial T}{\partial x}+v_{\mathrm{f},y}\frac{\partial T}{\partial y}\right)-\frac{T}{\rho}\frac{\partial \rho}{\partial T}\left(v_{\mathrm{f},x}\frac{\partial p}{\partial x}+v_{\mathrm{f},y}\frac{\partial p}{\partial y}\right) \\ &+\eta\left[\left(\frac{\partial v_{\mathrm{f},x}}{\partial z}\right)^2+\left(\frac{\partial v_{\mathrm{f},y}}{\partial z}\right)^2\right]=\rho c_p\frac{\partial T}{\partial t} \end{aligned} \tag{14}$$

and the solid bodies

$$\begin{aligned} &\frac{\partial}{\partial x}\left(\lambda_i\frac{\partial T}{\partial x}\right)+\frac{\partial}{\partial y}\left(\lambda_i\frac{\partial T}{\partial y}\right)+\frac{\partial}{\partial z}\left(\lambda_i\frac{\partial T}{\partial z}\right) \\ &-\rho_i c_{p,i}\left(v_{i,x}\frac{\partial T}{\partial x}+v_{i,y}\frac{\partial T}{\partial y}\right)=\rho_i c_{p,i}\frac{\partial T}{\partial t}\text{with } i=1,2 \end{aligned} \tag{15}$$

The definition of the heat flux density resulting from solid contact friction is defined according to Bobach et al. [36] as Eq. (16):

$$\begin{aligned} &\dot{q}_{\mathrm{f}} + k_{1;2}\left|(v_{1,x}-v_{2,x})\tau_{\mathrm{s}}\right| + k_{1;2}\left|(v_{1,y}-v_{2,y})\tau_{\mathrm{s}}\right| = \dot{q}_{1;2} \text{ with} \\ &\dot{q} = \lambda_{\mathrm{f};1;2}\frac{\partial T}{\partial z} \text{ and } k_{1;2} = 0.5 \end{aligned} \tag{16}$$

Thereby, the solid friction shear stress τ_{s} is calculated using the solid contact pressure p_{s} and the coefficient of solid friction μ_{s}.

$$\tau_{\mathrm{s}}(x,y,t) = \mu_{\mathrm{s}} \cdot p_{\mathrm{s}}(x,y,t) \tag{17}$$

For information on the boundary conditions in the thermal equations and additional details, the reader is referred to Farrenkopf et al. [27].

2.4.2 Calculation domains

All equations are implemented in a dimensionless formulation based on Habchi [33] and Farrenkopf et al. [27]. The resulting calculation domains are displayed in Fig. 3. The standard EHL calculation domain contains Ω_δ, Ω_T, and $\Omega_{T,1;2}$ (black). The extended EHL calculation domain includes $\Omega_{\delta,1;2}$, Ω_T, $\Omega_{T,1;2}$, $\Omega_{\delta,1;2,\mathrm{ext}}$, and $\Omega_{T,1;2,\mathrm{ext}}$ (black + blue).

The structural mechanics in Eq. (7) for the standard EHL calculation domain is solved on Ω_δ with $\sigma \cdot \vec{n} = p$ on Ω_{p}. The elastic deformation $\delta_{1,2}(x,y,t)$ corresponds to the displacement in z-direction on Ω_{p}. In the extended EHL calculation domain, Eq. (7) is solved on $\Omega_{\delta,1,(\mathrm{ext})}$ with $\sigma \cdot \vec{n} = p$ on Ω_{p}, and on $\Omega_{\delta,2,(\mathrm{ext})}$ with $\sigma \cdot \vec{n} = p$ on $\Omega_{p,2}$. Consequently, $\delta_1(x,y,t)$, and $\delta_2(x,y,t)$ are the displacements in z-direction on Ω_{p} and $\Omega_{p,2}$. Ω_{p} is utilized for solving the Reynolds equation (Eq. (7)) with $p = 0$ on $\partial\Omega_{\mathrm{p}}$, while the integration terms of Eq. (7) are solved on Ω_T. Equations (8)–(12) are also solved on Ω_T. The energy equation for the lubricant (Eq. (14)) is solved on Ω_T, while the energy equation of the two contact bodies (Eq. (15)) is solved on $\Omega_{T,1;2}$ in the standard EHL calculation domain and also on

$\Omega_{T,1;2,\mathrm{ext}}$ in case of the extended EHL calculation domain. The heat flux, resulting from solid contact friction (Eq. (16)), is applied on the boundary $\partial\Omega_{T,1;2}|_{z=0;h} = \partial\Omega_T|_{z=0;h}$.

2.4.3 Mixed lubrication

The influence of the surface topography on hydrodynamics is included using flow factor $\Phi^{\mathrm{p;s}}_{xx;yy}(h)$ [34, 35]. These flow factors characterize the influence of the surface topography on the Poiseuille and the Couette terms. To describe the solid contact, an integral solid contact pressure curve $p_\mathrm{s}(h)$ is used. It describes the correlation between the deformed gap height h and the solid contact pressure p_s of the elasto-plastic deformed rough surface contact. For the calculation of the solid contact pressure, the multilevel approach of Venner and Lubrecht [37] is used, deriving the integral solid contact pressure curve according to Bartel [29]. The study utilizes the same surface roughness measurements and the same pairings described in Farrenkopf et al. [27]. The surface roughness measurements were scaled to correspond to the measured R_a surface roughness parameter of the moderate low-loss gear (Section 2.1).

To consider the angle between the grinding direction and the line of contact, the angle β_B was applied to the surfaces. Figure 4 shows the aligned topographies of exemplary surfaces in the coordinate system of the contact line (x, y) and the original coordinate system of the measured raw data (x_0, y_0). The angle is $\beta_\mathrm{B} = 16.4°$ for the low-loss gear used.

Figure 5 displays the resulting flow factors and solid contact pressure curve.

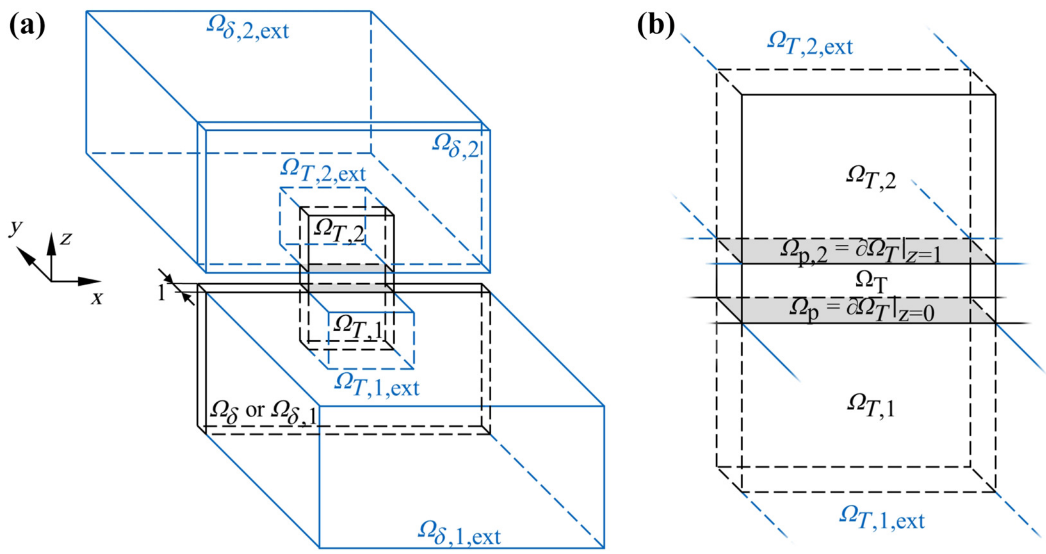

Fig. 3 (a) Total dimensionless calculation domains of the standard EHL calculation domain (black) and extended EHL calculation domain (black + blue) and (b) detailed view of the contact area.

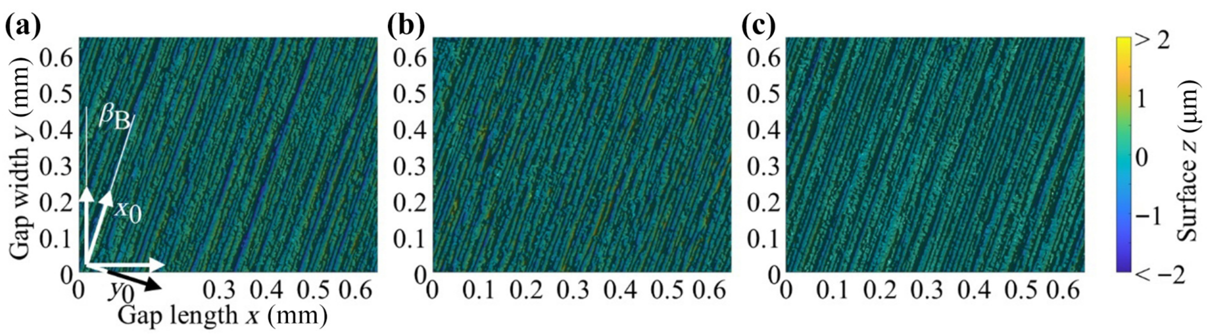

Fig. 4 Considered surface topographies of (a) tooth root, (b) tooth center, and (c) tooth tip area.

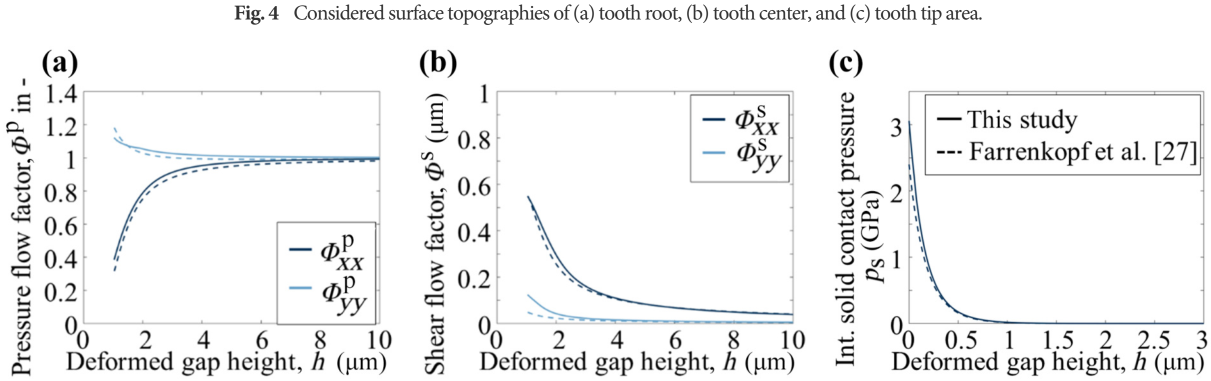

Fig. 5 (a) Pressure flow factors $\Phi^{\mathrm{p}}_{xx;yy}(h)$, (b) shear flow factors $\Phi^{\mathrm{s}}_{xx;yy}(h)$, and (c) integral solid contact pressure curve $p_\mathrm{s}(h)$ of Farrenkopf et al. [27] and the scaled/aligned configuration (this study).

2.4.4 Lubricant equation

The viscosity $\eta(T,p)$ as a function of temperature and pressure is described using the model of Roelands [38], whereby the temperature-dependent viscosity $\eta(T,p=0)$ is described by the equation of Vogel [39], Fulcher [40], and Tamman and Hesse [41]. The density $\rho(T,p)$ is modeled using the formulation of Bode [42], while the specific heat capacity $c_p(T,p)$ and the pressure dependency of the thermal conductivity $\lambda(p)$ follow Larsson and Andersson [43].

According to Eyring [44], the formulation is used to describe the non-Newtonian fluid behavior:

$$\dot{\gamma}=\frac{\tau_{\mathrm{C}}}{\eta}\cdot\sinh\left(\frac{\tau}{\tau_{\mathrm{C}}}\right) \tag{18}$$

There has been controversy [45–47] regarding the appropriate formulation for non-Newtonian fluid behavior. It is important to note that the non-Newtonian fluid model should be determined through viscometer measurements if possible. To ensure comparability and consistency, identical formulations to Farrenkopf et al. [27] are used for all lubricant equations and parameters, describing the ISO VG 100 mineral oil used. However, the literature also suggests a range of $\tau_{\mathrm{C}}=5-6$ MPa [1, 26, 48]. Therefore, a value of $\tau_{\mathrm{C}}=5.5$ MPa is used in this study, compared to $\tau_{\mathrm{C}}=3.8$ MPa used in Ref. [27]. It is important to note that other non-Newtonian fluid models are also applicable.

2.4.5 Numerical procedure

The numerical procedure is the same as that used in the author's previous work. First, the LTCA by RIKOR is performed for 90 contact lines to obtain the discretized parameter $f_{\mathrm{N}}(\bar{x},\bar{y})$, $v_{t,1;2}(\bar{x},\bar{y})$, and $\mathrm{corr}(\bar{x},\bar{y})$, as well as $h_{\mathrm{def}}(\bar{x},\bar{y})$ if needed. These data are then mapped into the coordinate system used for the TEHL model. The TEHL model, which is based on Habchi's [33] full-system approach, uses a direct solver to solve the fully coupled equation system in combination with the implicit backward Euler method. To counteract local element Peclet numbers $Pe^{\mathrm{e}}>1$, Galerkin Least Squares and Isotropic Diffusion are applied as stabilization techniques.

Figure 6 shows the results of the mesh sensitivity analysis in the extended EHL calculation domain, performed for $v_{t,\mathrm{C}}=8.3$ m/s at $t=1.39$ ms, which corresponds to the time step of maximum normal force F_{N}. The number of elements was varied between 7,221 and 94,193 elements, corresponding with a range of 59,348 and 1,108,250 degrees of freedom (dofs) for the tetrahedral and prismatic elements used.

Since the maximum hydrodynamic pressure p_{f}, maximum hydrodynamic shear stress τ_{f}, minimum and central lubricant film thickness h_{m} and h_{c}, and frictional power loss $P_{\mathrm{LGP},i}$ show convergence, 50,511 elements at 580,020 dofs are used.

2.5 Calculation of load-dependent gear power losses

The calculation of the load-dependent gear power losses refers to the cylindrical gears considered. According to Coulomb's law [49], the frictional power is

$$P=F_{\mathrm{N}}\cdot\mu\cdot v_{\mathrm{g}} \tag{19}$$

To calculate the time-averaged load-dependent gear power loss of a single tooth contact i, the equation of Farrenkopf et al. [27] can be used:

$$P_{\mathrm{LGP},i}=\frac{1}{t_{\mathrm{c}}}\cdot\int_0^{t_{\mathrm{c}}}P_{\mathrm{LGP},i}(t)\,\mathrm{d}t \tag{20}$$

Based on integrating the shear stresses and tangential velocities over the contact domain Ω_{p}, Eqs. (21)–(23) are used to evaluate the time-resolved fluid friction power loss $P_{\mathrm{L,f},i}(t)$, solid friction power losses $P_{\mathrm{L,s},i}(t)$, and load-dependent gear power losses $P_{\mathrm{LGP},i}(t)$ for a single contact line:

$$P_{\mathrm{L,f},i}(t)=\int_{\Omega_{\mathrm{p}}}\underbrace{\left(\tau_{\mathrm{f},zx}(x,y,t)|_{z=h/2}\cdot\left(v_{2,x}(y,t)-v_{1,x}(y,t)\right)\right)}_{\psi_{\Omega_{\mathrm{p,f},i}}(x,y,t)=P''_{\mathrm{L,f},i}(x,y,t)}\mathrm{d}x\mathrm{d}y \tag{21}$$

$$P_{\mathrm{L,s},i}(t)=\int_{\Omega_{\mathrm{p}}}\underbrace{\left(p_{\mathrm{s}}(x,y,t)\cdot\mu_{\mathrm{s}}\cdot\left(v_{2,x}(y,t)-v_{1,x}(y,t)\right)\right)}_{\psi_{\Omega_{\mathrm{p,s},i}}(x,y,t)=P''_{\mathrm{L,s},i}(x,y,t)}\mathrm{d}x\mathrm{d}y \tag{22}$$

$$P_{\mathrm{LGP},i}(t)=P_{\mathrm{L,f},i}(t)+P_{\mathrm{L,s},i}(t) \tag{23}$$

The time-resolved load-dependent gear power loss is the sum of all $P_{\mathrm{LGP},i}(t)$ for the maximum numbers of concurrent tooth flank contacts $\max(n(t))$:

$$\bar{P}_{\mathrm{LGP}}(t)=\sum_{i=1}^{\max n(t)}P_{\mathrm{LGP},i}\left(t+i\frac{1}{f_z}\right) \tag{24}$$

The time-averaged load-dependent gear power loss P_{LGP} reads

$$P_{\mathrm{LGP}}=\frac{1}{t_{\mathrm{c}}}\cdot\int_0^{t_{\mathrm{c}}}\bar{P}_{\mathrm{LGP}}(t)=\frac{\varepsilon_\gamma}{t_{\mathrm{c}}}\cdot\int_0^{t_{\mathrm{c}}}P_{\mathrm{LGP},i}(t) \tag{25}$$

Figure 17 illustrates that $P_{\mathrm{LGP}}(t)$ is periodic, so the contact time of a pair of teeth t_{c} (or an integer multiple) is used to calculate the time-average.

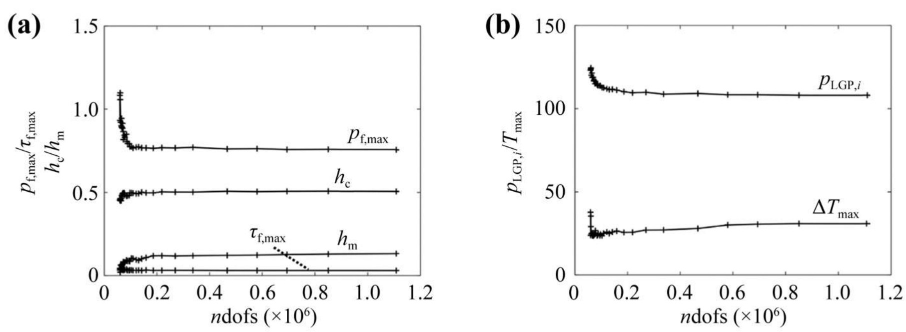

Fig. 6 Results of the mesh sensitivity analysis of the TEHL simulation model in the extended EHL calculation domain, performed for the highest maximum normal force F_{N} at $t=1.39$ ms.

3 Results and discussion

The TEHL modes are performed in the Cartesian coordinate system (x, y, z) shown in Fig. 7(a). The hydrodynamic pressure $p_{\mathrm{f}}(y,t)$, solid contact pressure $p_{\mathrm{f}}(y,t)$, and temperature rise $\Delta T(y,t)$ are evaluated for maximum values in the gap length direction (x-direction). The resulting curve along the gap width direction (y-direction) corresponds to a slice of the final representation plots. The slices are mapped according to their position in the tooth flank contact area, as defined by the time step t_i, as shown in Fig. 7(b).

The line load is calculated using the integral

$$f_{\mathrm{N}}(y,t) = \int_{x_{\mathrm{in}}}^{x_{\mathrm{out}}} \left(p_{\mathrm{f}}(x,y,t) + p_{\mathrm{s}}(x,y,t)\right) \mathrm{d}x \tag{26}$$

The linear friction power densities for a single tooth contact i are calculated by

$$P'_{\mathrm{L,f},i}(y,t) = \int_{x_{\mathrm{in}}}^{x_{\mathrm{out}}} \left(\tau_{\mathrm{f},zx}(x,y,t)|_{z=h/2} \cdot (v_{2,x}(y,t) - v_{1,x}(y,t))\right) \mathrm{d}x$$
$$P'_{\mathrm{L,s},i}(y,t) = \int_{x_{\mathrm{in}}}^{x_{\mathrm{out}}} (p_{\mathrm{s}}(x,y,t) \cdot \mu_{\mathrm{s}} \cdot (v_{2,x}(y,t) - v_{1,x}(y,t))) \mathrm{d}x \tag{27}$$

The distributions of the line load $f_{\mathrm{N}}(y,t)$, as well as the linear friction power densities $P'_{\mathrm{L,f},i}(\bar{x},\bar{y})$ and $P'_{\mathrm{L,s},i}(\bar{x},\bar{y})$ are then also mapped back into the tooth flank contact area.

As stated in Section 1, the objective of this work is to enhance the author's model [27], which is the reference. Based on that, the following Sections 3.1–3.7 present the results of improvements in a stepwise manner to eliminate assumptions and simplifications incrementally.

3.1 Reference

The reference has already been described and analyzed in detail in Ref. [27]. It is again presented in the following for further discussion and the sake of completion. Figure 8 shows for the reference the calculated (a) maximum hydrodynamic pressure $p_{\mathrm{f,max}}(\bar{x},\bar{y})$, (b) maximum solid contact pressure $p_{\mathrm{s,max}}(\bar{x},\bar{y})$, (c) maximum contact temperature rise $\Delta T_{\mathrm{max}}(\bar{x},\bar{y})$, (d) line load $f_{\mathrm{N}}(\bar{x},\bar{y})$, (e) linear fluid friction power density $P'_{\mathrm{L,f},i}(\bar{x},\bar{y})$, and (f) linear solid friction power density $P'_{\mathrm{L,s},i}(\bar{x},\bar{y})(\bar{x},\bar{y})$ over the tooth width $\bar{y}$ and line of action $\bar{x}$ for $T_1 = 208$ N·m, $v_{\mathrm{t,C}} = 8.3$ m/s, and $T_{\mathrm{oil}} = 363.15$ K in the standard EHL calculation domain with the accumulated deformation set to $h_{\mathrm{def}}(y,t) = 0$. The impact of tooth crowning is evident. Figure 8(a) shows a significant concentration of the maximum hydrodynamic pressure $p_{\mathrm{f,max}}(\bar{x},\bar{y})$ in the middle of the tooth width $\bar{y}$. A pressure ridge is formed near A and E in the tooth width direction $\bar{y}$. Since the hydrodynamic pressure is forced to be $p_{\mathrm{f}} = 0$ GPa at the beginning and the end of the contact line towards the tooth root and tip, the lubricant film thickness h decreases towards the beginning A and the end E of the line of action $\bar{x}$. Consequently,

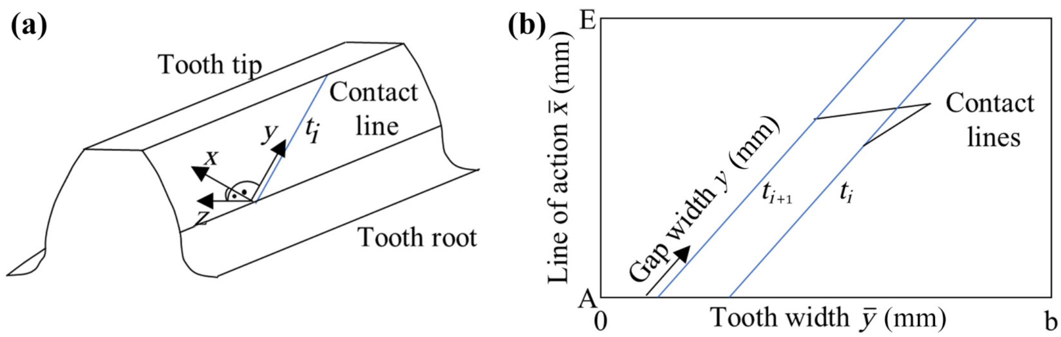

Fig. 7 Schematic contact line (a) on a gear tooth and (b) in the tooth flank contact area for the time step t_i.

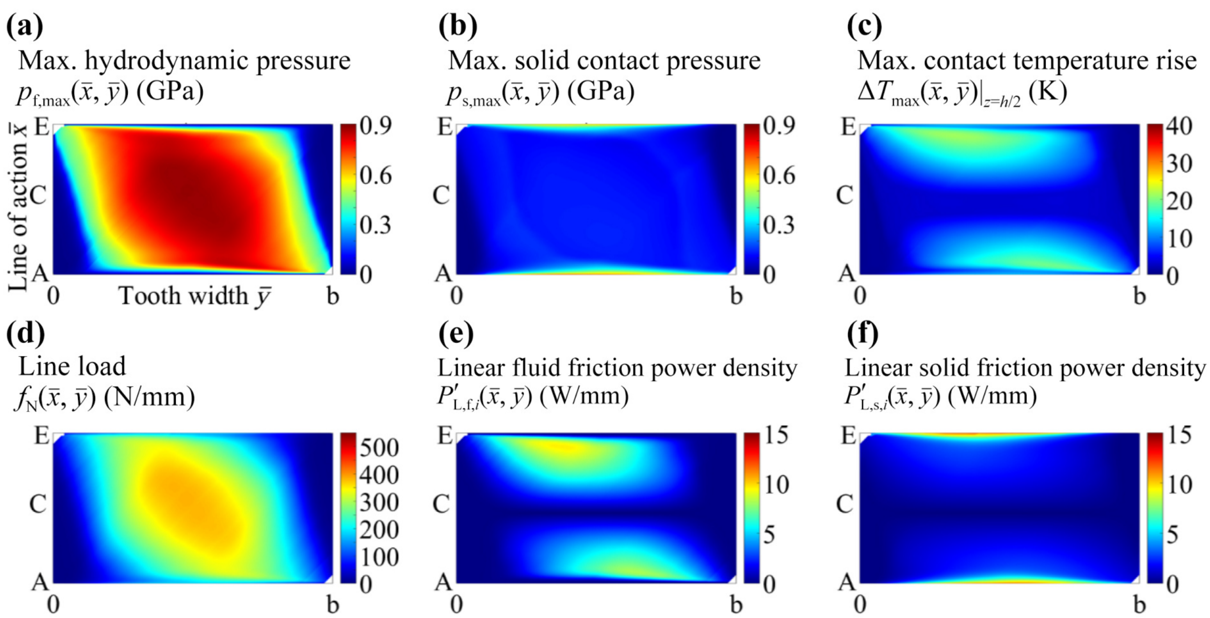

Fig. 8 (a) $p_{\mathrm{f,max}}(\bar{x},\bar{y})$, (b) $p_{\mathrm{s,max}}(\bar{x},\bar{y})$, (c) $\Delta T_{\mathrm{max}}(\bar{x},\bar{y})|_{z=h/2}$, (d) $f_{\mathrm{N}}(\bar{x},\bar{y})$, (e) $P'_{\mathrm{L,f},i}(\bar{x},\bar{y})$, and (f) $P'_{\mathrm{L,s},i}(\bar{x},\bar{y})$ for reference.

the solid contact pressure $p_{s,max}(\bar{x},\bar{y})$ in Fig. 8(b) is concentrated there. The line load $f_N(\bar{x},\bar{y})$ in Fig. 8(d) is strongly influenced by the hydrodynamic pressure. The hydrodynamic pressure distribution, resembling point contacts, causes a strong concentration of the line load $f_N(\bar{x},\bar{y})$ in the center of the tooth flank contact area. Figure 8(e) shows the linear fluid friction power density $P'_{L,f,i}(\bar{x},\bar{y})$, which is strongly linked to the hydrodynamic pressure but also superimposed by the sliding velocity. Therefore, the linear fluid friction power density $P'_{L,f,i}(\bar{x},\bar{y})$ is zero at the pitch point C and increases towards A and E. Its maximum values are attained at the pressure ridges described. In contrast, the linear solid friction power density $P'_{L,s,i}(\bar{x},\bar{y})$ in Fig. 8(f) is linked to the solid contact pressure. Thus, $P'_{L,s,i}(\bar{x},\bar{y})$ is subordinated in the midsection and increases slightly but steeply towards A and E. Both linear friction power densities directly affect the maximum contact temperature rise $\Delta T_{max}(\bar{x},\bar{y})$. Due to the dominance of the linear fluid friction power density $P'_{L,f,i}(\bar{x},\bar{y})$, the maximum contact temperature rise $\Delta T_{max}(\bar{x},\bar{y})$ follows its distribution over the tooth flank contact area, as shown in Fig. 8(c).

3.2 Influence of the accumulated system deformation

In this section, the accumulated deformation of the shaft-bearing system, the gear body, and the tooth $h_{def}(y,t)$, calculated in the LTCA (Section 2.2) and shown in Fig. 2(f) is added. Figure 9 shows the influence of accumulated system deformation on the calculated (a) maximum hydrodynamic pressure $p_{f,max}(\bar{x},\bar{y})$, (b) maximum solid contact pressure $p_{s,max}(\bar{x},\bar{y})$, (c) maximum contact temperature rise $\Delta T_{max}(\bar{x},\bar{y})$, (d) line load $f_N(\bar{x},\bar{y})$, (e) linear fluid friction power density $P'_{L,f,i}(\bar{x},\bar{y})$, and (f) linear solid friction power density $P'_{L,s,i}(\bar{x},\bar{y})$ over the tooth width $\bar{y}$ and line of action $\bar{x}$ for $T_1 = 208$ N·m, $v_{t,C} = 8.3\ \mathrm{m/s}$, and $T_{oil} = 363.15$ K in the standard EHL calculation domain. The greatest accumulated deformation of the shaft-bearing system, the gear body, and the tooth $h_{def}(y,t)$ occurs at points with high tooth crowning. This results in the maximum hydrodynamic pressure distribution $p_{f,max}(\bar{x},\bar{y})$ of Fig. 9(a) evolving more towards a line contact, which eliminates low-loaded regions of the tooth flank contact area. The expanded pressure distribution leads to a reduction in the maximum pressure level. Another effect is the formation of more pronounced pressure ridges, which extend further towards the center of the tooth width $\bar{y}$. In Fig. 9(b), the maximum solid contact pressure $p_{s,max}(\bar{x},\bar{y})$ and, therefore, also the linear solid friction power density $P'_{L,s,i}(\bar{x},\bar{y})$ in Fig. 9(f) show no remarkable changes compared to the reference. The distribution of the linear fluid friction power density $P'_{L,f,i}(\bar{x},\bar{y})$ in Fig. 9(e) demonstrates the effect of the shifted pressure ridge in combination with a decreased pressure level, which has the same impact on the maximum contact temperature rise $\Delta T_{max}(\bar{x},\bar{y})$ in Fig. 9(c).

3.3 Influence of the scaled and aligned surface topography

Figure 10 shows the influence of scaled and aligned surface topography on the calculated (a) maximum hydrodynamic pressure $p_{f,max}(\bar{x},\bar{y})$, (b) maximum solid contact pressure $p_{s,max}(\bar{x},\bar{y})$, (c) maximum contact temperature rise $\Delta T_{max}(\bar{x},\bar{y})$, (d) line load $f_N(\bar{x},\bar{y})$, (e) linear fluid friction power density $P'_{L,f,i}(\bar{x},\bar{y})$, and (f) linear solid friction power density $P'_{L,s,i}(\bar{x},\bar{y})$ over the tooth width $\bar{y}$ and line of action $\bar{x}$ for $T_1 = 208$ N·m, $v_{t,C} = 8.3\ \mathrm{m/s}$, and $T_{oil} = 363.15$ K in the standard EHL calculation domain. The flow factors $\Phi^{p;s}_{xx;yy}(h)$ and the integral solid contact pressure curve $p_s(h)$ of Farrenkopf et al. [27] are replaced by the ones derived in Section 2.4.3, which consider the scaled and aligned surface topography and directly influence the pressure distributions. Figure 10(b) shows that the maximum solid contact pressure $p_{s,max}(\bar{x},\bar{y})$ is slightly higher in the mid-section of the tooth flank contact area than in Section 3.2. In Fig. 10(a), the maximum hydrodynamic pressure $p_{f,max}(\bar{x},\bar{y})$ in has a slightly decreased level, except for the pressure ridges near A and E. As a result, the line load distribution $f_N(\bar{x},\bar{y})$ in Fig. 10(d) remains nearly unchanged. The linear fluid friction power density $P'_{L,f,i}(\bar{x},\bar{y})$ in Fig. 10(e) is influenced by the changes in hydrodynamic pressure. This results in a constant level at the ridges but a steeper decrease towards the pitch point C. In Fig. 10(f), the linear solid friction power density $P'_{L,s,i}(\bar{x},\bar{y})$ increased negligibly as changes in the mid-section of solid contact pressure are superimposed by small sliding velocities $|v_{1,x}(y,t) - v_{2,x}(y,t)|$ near the pitch point C. The small variations in the maximum contact temperature rise $\Delta T_{max}(\bar{x},\bar{y})$ shown in Fig. 10(f) are only slightly affected by friction power densities.

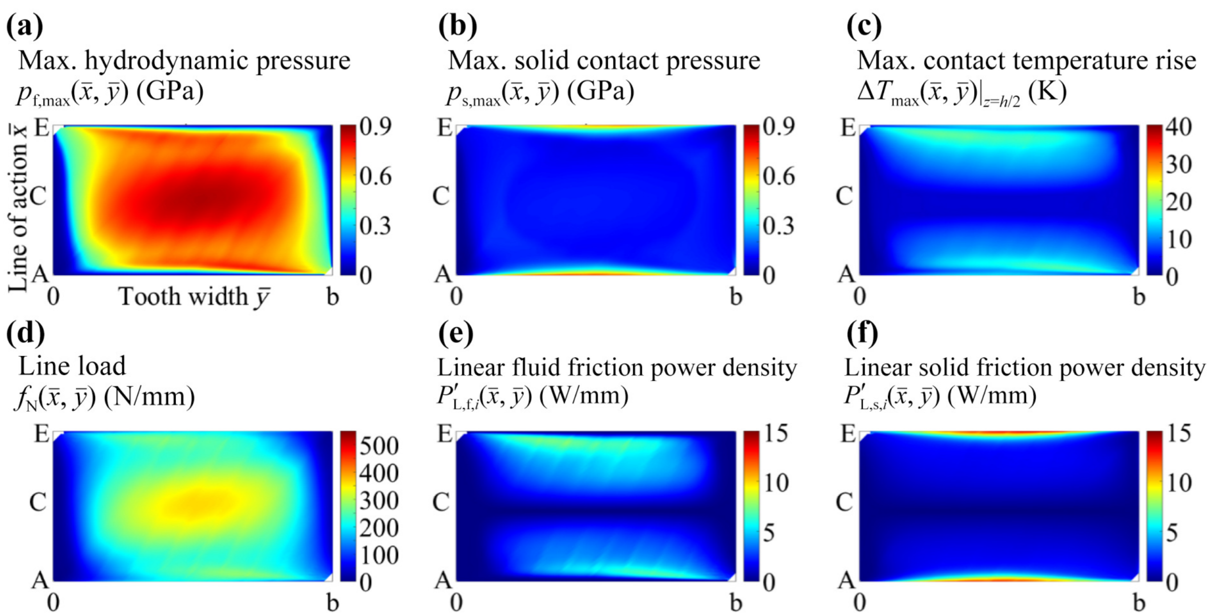

Fig. 9 Influence of the accumulated system deformation: (a) $p_{f,max}(\bar{x},\bar{y})$, (b) $p_{s,max}(\bar{x},\bar{y})$, (c) $\Delta T_{max}(\bar{x},\bar{y})|_{z=h/2}$, (d) $f_N(\bar{x},\bar{y})$, (e) $P'_{L,f,i}(\bar{x},\bar{y})$, and (f) $P'_{L,s,i}(\bar{x},\bar{y})$.

3.4 Influence of the gear bulk temperature

Figure 11 shows for the influence of the gear bulk temperature on the calculated (a) maximum hydrodynamicpressure $p_{\mathrm{f,max}}(\bar{x},\bar{y})$, (b) maximum solid contact pressure $p_{\mathrm{s,max}}(\bar{x},\bar{y})$, (c) maximum contact temperature rise $\Delta T_{\max}(\bar{x},\bar{y})$, (d) line load $f_{\mathrm{N}}(\bar{x},\bar{y})$, (e) linear fluid friction power density $P'_{\mathrm{L,f},i}(\bar{x},\bar{y})$, and (f) linear solid friction power density $P'_{\mathrm{L,s},i}(\bar{x},\bar{y})$ over the tooth width $\bar{y}$ and line of action $\bar{x}$ for $T_1 = 208$ N·m, $v_{\mathrm{t,C}} = 8.3$ m/s, and $T_{\mathrm{oil}} = 363.15$ K in the standard EHL calculation domain. The bulk temperature considered is set to be $T_{\mathrm{M}} = 366.1$ K, which is calculated according to Section 2.3 and defined as a boundary condition. It is important to note that the oil inlet temperature remains at $T_{\mathrm{oil}} = 363.15$ K and serves as the reference value of the maximum contact temperature rise $\Delta T_{\max}(\bar{x},\bar{y})$. An increase in temperature level leads to a decrease in viscosity $\eta(T,p)$, which results to a slight decrease in the maximum hydrodynamic pressure $p_{\mathrm{f,max}}(\bar{x},\bar{y})$ level (Fig. 11(a)). Simultaneously, the decrease in viscosity causes a reduction in the lubricant film thickness, resulting in a higher solid contact pressure $p_{\mathrm{s,max}}(\bar{x},\bar{y})$, as shown in Fig. 11(b). This increase affects the entire tooth flank contact area, but particularly the edges A and E. In terms of line load $f_{\mathrm{N}}(\bar{x},\bar{y})$ in Fig. 11(d), these effects almost cancel each other out. The influence on the linear friction power densities $P'_{\mathrm{L,f},i}(\bar{x},\bar{y})$ in Fig. 11(e) and $P'_{\mathrm{L,s},i}(\bar{x},\bar{y})$ in Fig. 11(f) is barely noticeable, except for a lower linear fluid friction power density $P'_{\mathrm{L,f},i}(\bar{x},\bar{y})$ at the pressure ridges. Thus, the maximum contact temperature rise $\Delta T_{\max}(\bar{x},\bar{y})$ in Fig. 11(c) is mainly influenced by the higher bulk temperature T_{M} level.

3.5 Influence of the coefficient of solid friction

Figure 12 shows the influence of the coefficient of solid friction on the calculated (a) maximum hydrodynamicpressure $p_{\mathrm{f,max}}(\bar{x},\bar{y})$,

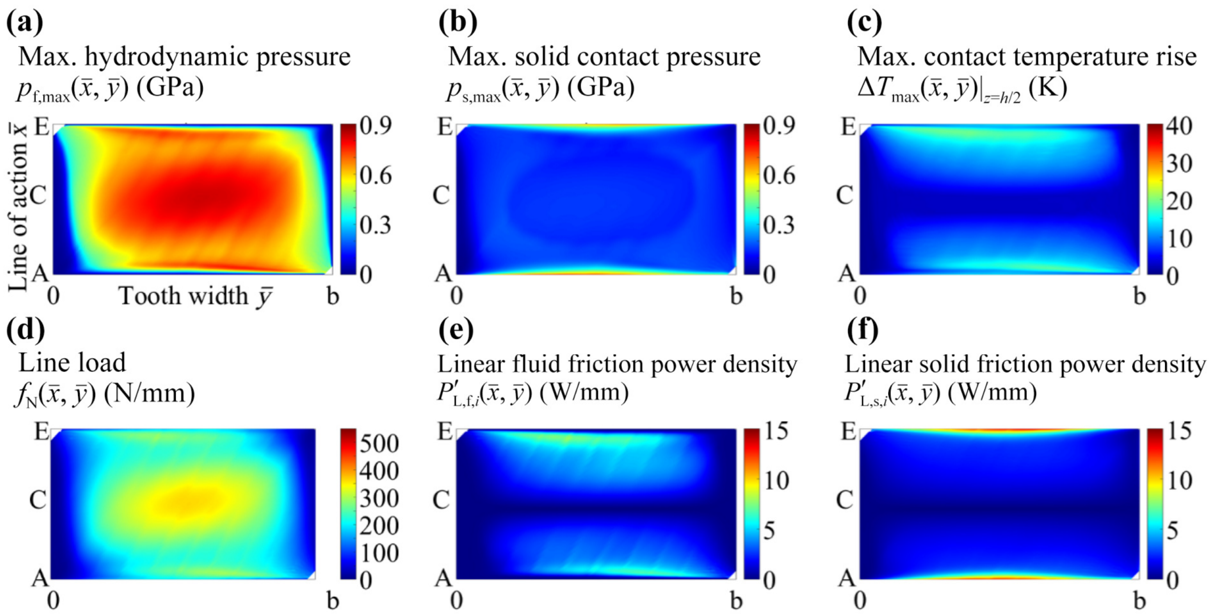

Fig. 10 Influence of the scaled and aligned surface topography: (a) $p_{\mathrm{f,max}}(\bar{x},\bar{y})$, (b) $p_{\mathrm{s,max}}(\bar{x},\bar{y})$, (c) $\Delta T_{\max}(\bar{x},\bar{y})|_{z=h/2}$, (d) $f_{\mathrm{N}}(\bar{x},\bar{y})$, (e) $P'_{\mathrm{L,f},i}(\bar{x},\bar{y})$, and (f) $P'_{\mathrm{L,s},i}(\bar{x},\bar{y})$.

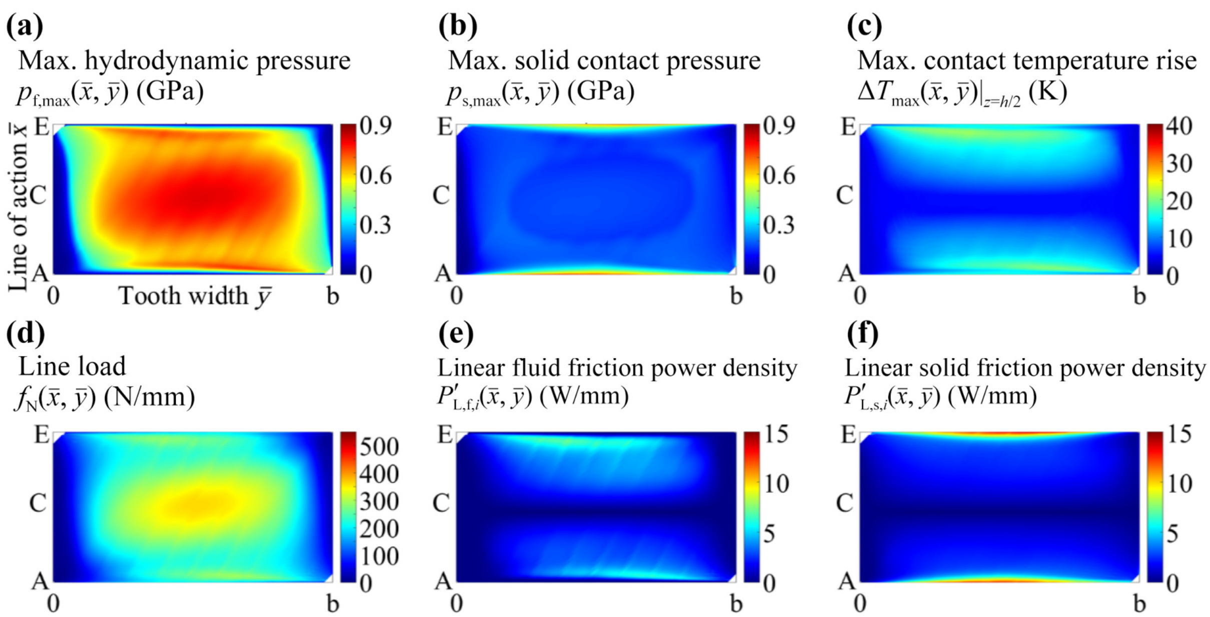

Fig. 11 Influence of the gear bulk temperature: (a) $p_{\mathrm{f,max}}(\bar{x},\bar{y})$, (b) $p_{\mathrm{s,max}}(\bar{x},\bar{y})$, (c) $\Delta T_{\max}(\bar{x},\bar{y})|_{z=h/2}$, (d) $f_{\mathrm{N}}(\bar{x},\bar{y})$, (e) $P'_{\mathrm{L,f},i}(\bar{x},\bar{y})$, and (f) $P'_{\mathrm{L,s},i}(\bar{x},\bar{y})$.

(b) maximum solid contact pressure $p_{\mathrm{s,max}}(\bar{x},\bar{y})$, (c) maximum contact temperature rise $\Delta T_{\max}(\bar{x},\bar{y})$, (d) line load $f_{\mathrm{N}}(\bar{x},\bar{y})$, (e) linear fluid friction power density $P'_{\mathrm{L,f},i}(\bar{x},\bar{y})$, and (f) linear solid friction power density $P'_{\mathrm{L,s},i}(\bar{x},\bar{y})$ over the tooth width $\bar{y}$ and line of action $\bar{x}$ for $T_1 = 208$ N·m, $v_{\mathrm{t,C}} = 8.3$ m/s, and $T_{\mathrm{oil}} = 363.15$ K in the standard EHL calculation domain. In the previous studies, a coefficient of solid friction $\mu_{\mathrm{s}} = 0.05$ was used. In the following, $\mu_{\mathrm{s}} = 0.08$ is applied as explained in Section 2.1.

$p_{\mathrm{f,max}}(\bar{x},\bar{y})$ in Fig. 12(a), $p_{\mathrm{s,max}}(\bar{x},\bar{y})$ in Fig. 12(b), $f_{\mathrm{N}}(\bar{x},\bar{y})$ in Fig. 12(d), and $P'_{\mathrm{L,f},i}(\bar{x},\bar{y})$ in Fig. 12(e) are nearly unaffected. However, linear solid friction power density $P'_{\mathrm{L,s},i}(\bar{x},\bar{y})$ in Fig. 12(f) is more strongly affected, showing a steeper increase from the pitch point C towards A and E, and a substantial increase at A and E. This results in a second set of temperature maxima directly at the edge at A and C, shown in Fig. 12(c). Since the hydrodynamic pressure p_{f} is set to zero at A and E, the temperature increase has a limited influence on the hydrodynamic and solid contact pressure p_{f} and p_{s}.

3.6 Influence of the tooth stiffness

Up to this point, the model is based on two cylindrical contact bodies with parallel axes and equal length (standard EHL calculation domain). The faces at the end of the cylinders significantly affect primarily the structural mechanics (Eq. (6)), and, secondarily, the lubricant film thickness and also the remaining hydrodynamics. However, when considering a contact line of a helical gear contact, this contact line begins near the root of one tooth and the tip of the other tooth of the two gears at A, as shown in Fig. 7(a). The end of the contact line at E shows the opposite behavior. To consider the influence of the tooth root, the domain of structural mechanics is extended, as shown in Fig. 3. The resulting asymmetry makes it impossible to substitute into an equivalent system. Therefore, structural mechanics is now computed on both domains $\Omega_{\delta,1}$ and $\Omega_{\delta,2}$, as well as their extensions $\Omega_{\delta,1;2,\mathrm{ext}}$. Since the tooth root also affects heat conduction, the domains $\Omega_{T,1}$ and $\Omega_{T,1}$ are extended by $\Omega_{T,1;2,\mathrm{ext}}$.

Figure 13 shows the influence of tooth stiffness on the calculated (a) maximum hydrodynamicpressure $p_{\mathrm{f,max}}(\bar{x},\bar{y})$, (b) maximum solid contact pressure $p_{\mathrm{s,max}}(\bar{x},\bar{y})$, (c) maximum contact temperature rise $\Delta T_{\max}(\bar{x},\bar{y})$, (d) line load $f_{\mathrm{N}}(\bar{x},\bar{y})$, (e) linear fluid friction power density $P'_{\mathrm{L,f},i}(\bar{x},\bar{y})$, and (f) linear solid friction power density $P'_{\mathrm{L,f},i}(\bar{x},\bar{y})$ over the tooth width $\bar{y}$ and line of action $\bar{x}$ for $T_1 = 208$ N·m, $v_{\mathrm{t,C}} = 8.3$ m/s, and $T_{\mathrm{oil}} = 363.15$ K in the extended EHL calculation domain.

As anticipated, the maximum solid contact pressure $p_{\mathrm{s,max}}(\bar{x},\bar{y})$ in Fig. 13(b) increases significantly at the edges E and A. Similarly, in Fig. 13(a), the maximum hydrodynamic pressure $p_{\mathrm{f,max}}(\bar{x},\bar{y})$ is also affected near the edges, leading to increased pressure ridges. To maintain force balance, the hydrodynamic pressure $p_{\mathrm{f,max}}(\bar{x},\bar{y})$ is reduced in the mid-section around the pitch point C. Accordingly, the linear friction power densities $P'_{\mathrm{L,f},i}(\bar{x},\bar{y})$ and $P'_{\mathrm{L,s},i}(\bar{x},\bar{y})$ in Figs. 13(e) and 13(f) follow the trends of the hydrodynamic and solid contact pressure. As a result, there is a significant increase in the temperature maxima (Fig. 13(c)).

3.7 Influence of the Eyring shear stress

Figure 14 shows for the influence of the Eyring shear stress on the calculated (a) maximum hydrodynamicpressure $p_{\mathrm{f,max}}(\bar{x},\bar{y})$, (b) maximum solid contact pressure $p_{\mathrm{s,max}}(\bar{x},\bar{y})$, (c) maximum contact temperature rise $\Delta T_{\max}(\bar{x},\bar{y})$, (d) line load $f_{\mathrm{N}}(\bar{x},\bar{y})$, (e) linear fluid friction power density $P'_{\mathrm{L,f},i}(\bar{x},\bar{y})$, and (f) linear solid friction power density $P'_{\mathrm{L,s},i}(\bar{x},\bar{y})$ over the tooth width $\bar{y}$ and line of action $\bar{x}$ for $T_1 = 208$ N·m, $v_{\mathrm{tC}} = 8.3$ m/s, and $T_{\mathrm{oil}} = 363.15$ K in the extended EHL calculation domain. In the previous studies, an Eyring shear stress $\tau_{\mathrm{C}} = 3.8$ MPa was used. In this study $\tau_{\mathrm{C}} = 5.5$ MPa is applied as explained in Section 2.4.4.

While the hydrodynamic pressure $p_{\mathrm{f,max}}(\bar{x},\bar{y})$ slightly increases in the ridges in Fig. 14(a), $P'_{\mathrm{L,f},i}(\bar{x},\bar{y})$ in Fig. 14(e) increases significantly there. $p_{\mathrm{s,max}}(\bar{x},\bar{y})$ in Fig. 14(b), $f_{\mathrm{N}}(\bar{x},\bar{y})$ in Fig. 14(d), and $P'_{\mathrm{L,s},i}(\bar{x},\bar{y})$ in Fig. 14(f) are barely affected. The increase in temperature is solely influenced by the increase in fluid friction, as shown Fig. 14(c).

3.8 Combined influence on load-dependent gear power loss

In Fig. 15(a), the load-dependent gear power loss $P_{\mathrm{LGP,i}}(t)$ of a single tooth contact i (Eq. (20)) is compared for the influences investigated in Sections 3.1–3.7 at $T_1 = 208\ \mathrm{N\cdot m}$, $v_{\mathrm{t,C}} = 8.3$m/s, and $T_{\mathrm{oil}} = 363.15$ K. Additionally, for better visualization, the

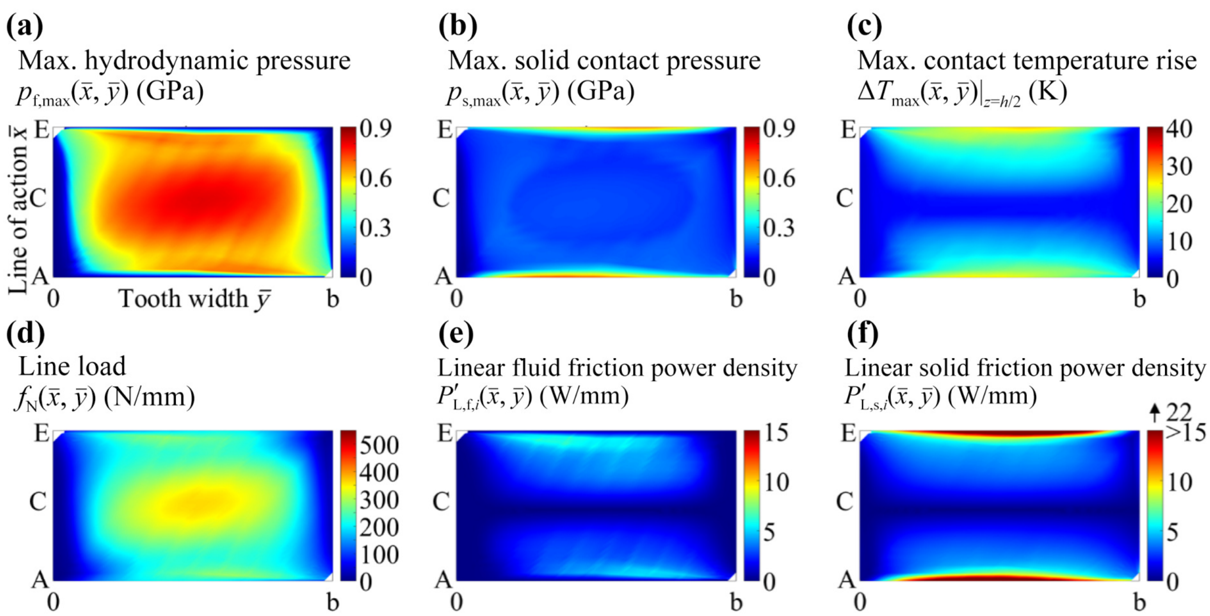

Fig. 12 Influence of the coefficient of solid friction: (a) $p_{\mathrm{f,max}}(\bar{x},\bar{y})$, (b) $p_{\mathrm{s,max}}(\bar{x},\bar{y})$, (c) $\Delta T_{\max}(\bar{x},\bar{y})|_{z=h/2}$, (d) $f_{\mathrm{N}}(\bar{x},\bar{y})$, (e) $P'_{\mathrm{L,f},i}(\bar{x},\bar{y})$, and (f) $P'_{\mathrm{L,s},i}(\bar{x},\bar{y})$.

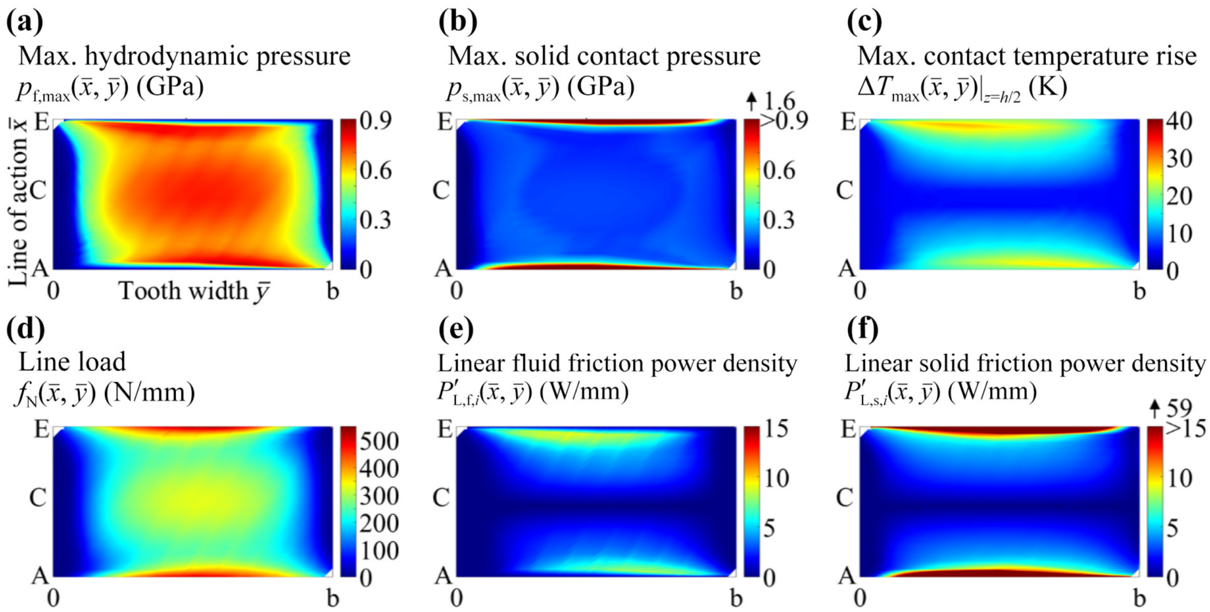

Fig. 13 Influence of the tooth stiffness: (a) $p_{\mathrm{f,max}}(\bar{x},\bar{y})$, (b) $p_{\mathrm{s,max}}(\bar{x},\bar{y})$, (c) $\Delta T_{\mathrm{max}}(\bar{x},\bar{y})\,|_{z=h/2}$, (d) $f_{\mathrm{N}}(\bar{x},\bar{y})$, (e) $P'_{\mathrm{L,f},i}(\bar{x},\bar{y})$, and (f) $P'_{\mathrm{L,s},i}(\bar{x},\bar{y})$.

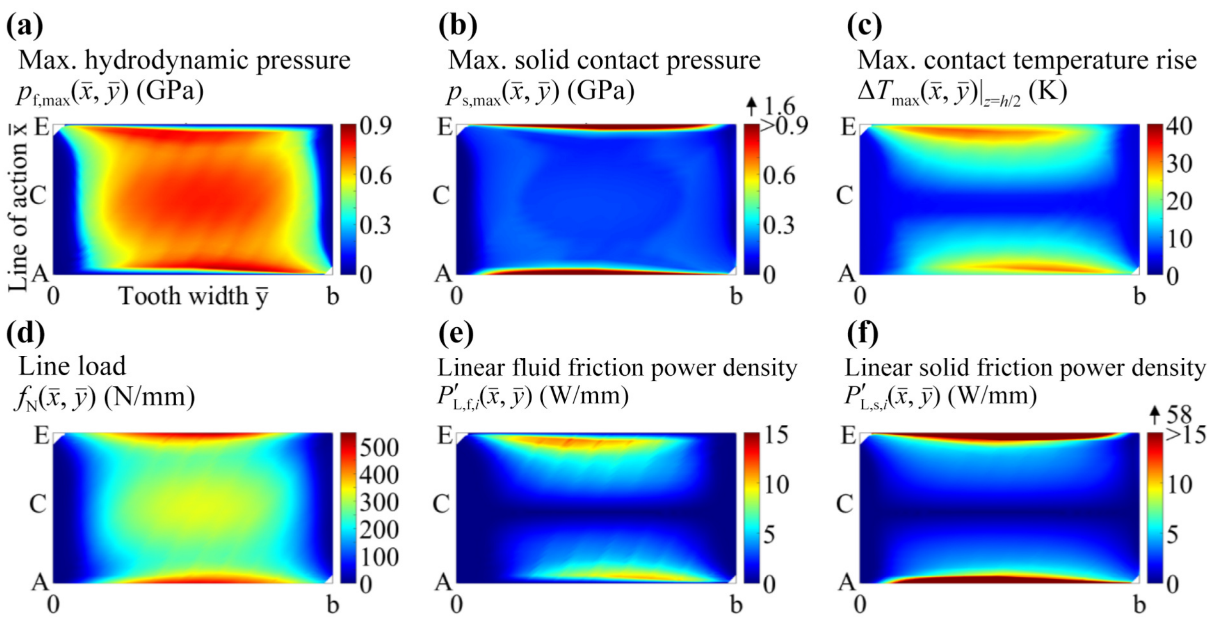

Fig. 14 Influence of the Eyring shear stress: (a) $p_{\mathrm{f,max}}(\bar{x},\bar{y})$, (b) $p_{\mathrm{s,max}}(\bar{x},\bar{y})$, (c) $\Delta T_{\mathrm{max}}(\bar{x},\bar{y})\,|_{z=h/2}$, (d) $f_{\mathrm{N}}(\bar{x},\bar{y})$, (e) $P'_{\mathrm{L,f},i}(\bar{x},\bar{y})$, and (f) $P'_{\mathrm{L,s},i}(\bar{x},\bar{y})$.

relative load-dependent gear power losses ζ_{LGP} (Eq. (25)) are also shown in Fig. 15(b).

Based on the reference, the accumulated system deformation $h_{\mathrm{def}}(y,t)$ leads to a more centered and slightly lowered curve of the fluid friction power loss $P_{\mathrm{L,f},i}(t)$, following the linear fluid friction power density $P'_{\mathrm{L,f},i}(\bar{x},\bar{y})$ in Fig. 9(e). It is overlaid by a marginally higher solid friction power loss $P_{\mathrm{L,s},i}(t)$ (Fig. 15(b)). These effects result in a more centered total friction power loss curve $P_{\mathrm{LGP},i}(t)$ in Fig. 15(a) and a similar relative load-dependent gear power loss ζ_{LGP}, as shown in Fig. 15(b). The low-loss gear geometry and the setup of the FZG efficiency test rig result in small overall deformation. Much higher deformations are expected in other applications, such as automotive [50].

The curves of the scaled and aligned surface topography and the adapted gear bulk temperature on the fluid friction power loss $P_{\mathrm{L,f}}$ are slightly decreasing, and solid friction power loss $P_{\mathrm{L,s}}$ are slightly increasing, respectively. These effects cancel each other out (Fig. 15(b)). Note that the selected gear has a low-loss geometry, resulting in relatively low load-dependent gear power losses. Therefore, the temperature rise in the bulk material is also relatively low (Section 2.3). When using different gear geometries, higher rotational speeds, or different lubrication methods, a more significant influence is expected [3, 51, 52]. In addition, the difference in roughness compared to the reference is small. Other surface treatments, such as superfinishing, stream finishing, or surface texturing, can have a significant effect [2].

The influence of the coefficient of solid friction on the fluid friction power loss $P_{\mathrm{L,f}}$ is insignificant, as expected based on the findings of Section 3.5. In contrast, the solid friction power loss $P_{\mathrm{L,s}}$, shows a significant increase, resulting in a consequent increase of the load-dependent gear power loss $P_{\mathrm{LGP},i}(t)$ in Fig. 15(a) and the relative load-dependent gear power loss ζ_{LGP} in

Fig. 15(b). The coefficient of solid friction can vary significantly and can be strongly influenced by surface-active lubricant additives, surface properties, and coatings [53].

The influence of the tooth root has a slight impact on the fluid friction power loss $P_{\mathrm{L,f}}$, but significantly increase the solid friction power loss $P_{\mathrm{L,s}}$. As described in Section 3.6, the impact of tooth stiffness of the root is most significant at the edges A and E. These areas also experience the highest sliding velocities, resulting in a more pronounced increase in solid friction and a greater effect on the load-dependent gear power loss $P_{\mathrm{LGP},i}(t)$ and relative load-dependent gear power loss ζ_{LGP} in Figs. 15(a) and 15(b), respectively.

The Eyring shear stress has a negligible effect on the solid friction power loss $P_{\mathrm{L,s}}$. In contrast, in has a clear impact on fluid friction, leading to an increase in the fluid friction power loss $P_{\mathrm{L,f}}$ and, consequently, an increase in the load-dependent gear power loss $P_{\mathrm{LGP},i}$ in Fig. 15(a). Additionally, the fluid friction share of the relative load-dependent gear power loss ζ_{LGP} increases as depicted in Fig. 15(b).

For the final calculation setup of Section 3.7 at $v_{\mathrm{t,C}} = 8.3\ \mathrm{m/s}$, the total frictional power density $\psi_{\Omega_{\mathrm{p},i}}$ is shown in Fig. 16. The three time steps $t = \{0.1 \cdot t_{\mathrm{c}}, 0.5 \cdot t_{\mathrm{c}}, 0.9 \cdot t_{\mathrm{c}}\}\ \mathrm{s}$ are the same time steps shown in Ref. [27]. Comparing both, it can be noted for all three time steps that the total frictional power density $\psi_{\Omega_{\mathrm{p},i}}$ at loaded edges has increased significantly while the mid-section is barely effected. As explained, the main reasons are the adapted coefficient of solid friction in Section 3.5 and the influence of the tooth root in Section 3.6.

3.9 Comparison with experimental results

To evaluate the accuracy and quality of the current simulation, the numerical results are compared with Hinterstoißer's [2] experimentally measured load-dependent gear power losses $P_{\mathrm{LGP,exp}}$. Figure 17 shows the load-dependent gear power losses for the final calculation setup in Section 3.7 at $v_{\mathrm{t,C}} = 8.3\ \mathrm{m/s}$. The load-dependent gear power losses of each tooth contact $P_{\mathrm{LGP},i}(t)$ are parabolic in shape, and each is shifted by $\Delta t = 1/f_z$. Equation (24) is used to sum up all contact lines, resulting in the time-resolved, load-dependent gear power loss $\bar{P}_{\mathrm{LGP}}(t)$. P_{LGP} represents the time-average of $\bar{P}_{\mathrm{LGP}}(t)$, described by Eq. (25). This average value is then compared to measurement results $P_{\mathrm{LGP,exp}}$ of Hinterstoißer [28]. Please note that the value of Hinterstoißer also corresponds to a time-average, and measurements are also affected by a tolerance. A difference of 7.8% is obtained.

Please note the oscillating load-dependent gear power loss $\bar{P}_{\mathrm{LGP}}(t)$ is neglected using mesh-averaged approaches, while the amplitude varies with the gear geometry and frequency with rotational speed.

Besides $v_{\mathrm{t,C}} = 8.3\ \mathrm{m/s}$, the circumferential speeds of $v_{\mathrm{t,C}} = 2\ \mathrm{m/s}$ and $v_{\mathrm{t,C}} = 20\ \mathrm{m/s}$ are also computed in this study using the calculation setup of Section 3.7. The gear tooth bulk temperatures T_{M} is adapted according to the considered circumferential speeds $v_{\mathrm{t,C}}$ as explained in Section 2.3. Figure 18 shows a comparison of the simulation results with the measurement results of Hinterstoißer [2]. Both show a very good correlation across the considered operating points. Nevertheless, the offset slightly increases towards smaller pitch line velocities. Remaining simplifications, like the mixed lubrication approach and the literature values for Eyring shear stress τ_{c} and the coefficient of solid friction μ_{s}, can be improved to further increase the quality of the results.

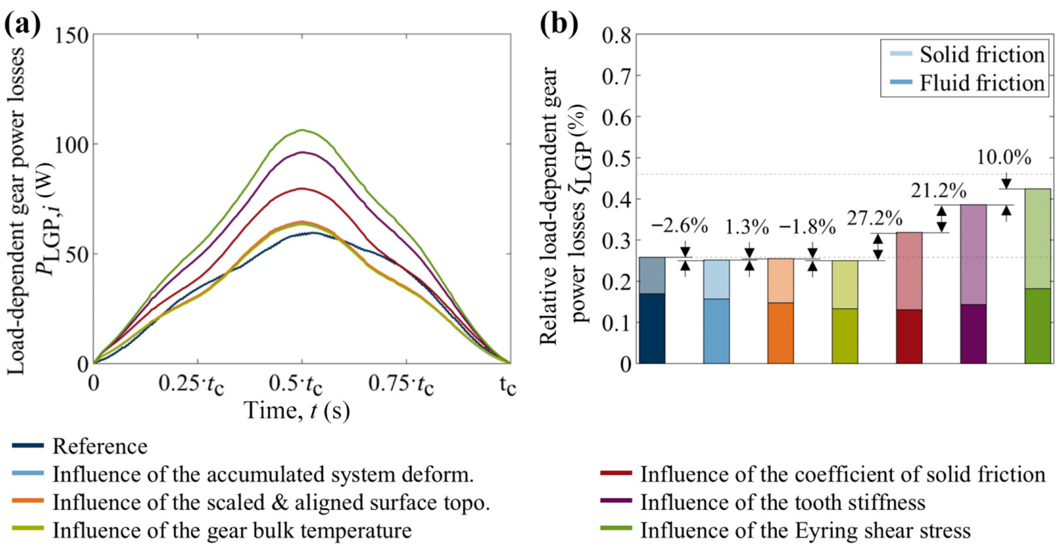

Fig. 15 (a) $P_{\mathrm{LGP},i}(t)$ of a single tooth contact i and overall (b) ζ_{LGP} of the reference and the influence studies in Sections 3.1–3.7.

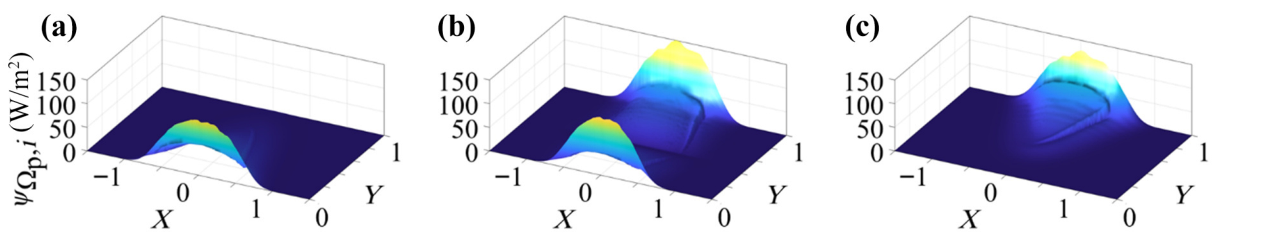

Fig. 16 Total frictional power density $\psi_{\Omega_{\mathrm{p},i}}$ along the contact line for $T_1 = 208\ \mathrm{N \cdot m}$, $v_{\mathrm{t,C}} = 8.3\ \mathrm{m/s}$ and $T_{\mathrm{oil}} = 363.15\ \mathrm{K}$ at three time steps $t = \{0.1 \cdot t_{\mathrm{c}}, 0.5 \cdot t_{\mathrm{c}}, 0.9 \cdot t_{\mathrm{c}}\}$.

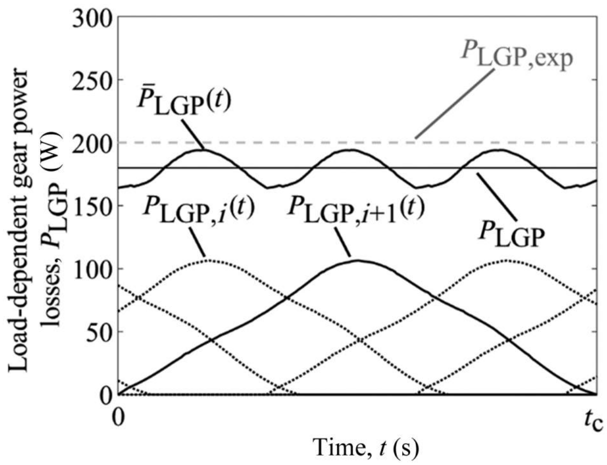

Fig. 17 P_{LGP}, $\bar{P}_{LGP}(t)$, and $P_{LGP,i}(t)$, compared with experimental measurements $P_{LGP,exp}$ of Hinterstoißer [28] along the contact time for $T_1 = 208$ N·m, $v_{t,C} = 8.3$ m/s and $T_{oil} = 363.15$ K.

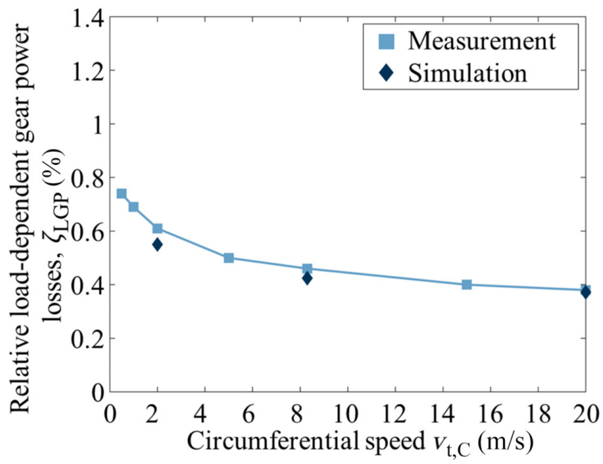

Fig. 18 Relative load-dependent gear power loss ζ_{LGP} of the low-loss gear ($T_1 = 208$ N·m, $T_{oil} = 363.15$ K) measured by Hintersoißer [2] compared with simulation results at $v_{t,C} = \{2, 8.3, 20\}$ m/s.

4 Conclusions

This study presents a model to calculate and predict load-dependent gear power loss of cylindrical gears using a TEHL model, including mixed lubrication. The results are compared with experimental results and show a very good correlation. Several simplifications were eliminated in a stepwise study to show the influence. The main conclusions are:

(1) The accumulated deformation from bearings, shafts, the gear body, and the teeth shows changes in the load distribution, but minor influence on the load-dependent gear power loss ($\Delta\zeta_{LGP} = -2.6\%$). Softer gear geometries and softer shafts, housing and bearing systems than considered can cause more significant changes;

(2) The grinding direction and an increase in surface roughness from Ra = 0.135 μm by 41% have minor influence on the load-dependent gear power loss ($\Delta\zeta_{LGP} = +1.3\%$) for the operating conditions considered;

(3) The consideration of the bulk temperature has also a minor influence on the load-dependent gear power loss ($\Delta\zeta_{LGP} = -1.8\%$). This is because the bulk temperature increase compared to the oil temperature is very small for the considered low-loss gear geometry. Other gear geometries can lead to significantly greater effects;

(4) The coefficient of solid friction μ_s has a strong influence on the load-dependent power loss ($\Delta\zeta_{LGP} = +27.2\%$). This underlines the relevance of measures like coatings or lubricant additives to reduce the coefficient of solid friction;

(5) The consideration of tooth root stiffness and heat conduction has a significant influence on the solid contact pressure at the begin and end of a contact line at the edges towards the tooth root and tip and influences the load-dependent gear power loss accordingly ($\Delta\zeta_{LGP} = +21.2\%$);

(6) The parameters of non-Newtonian fluid models have a significant influence on load-dependent gear power loss ($\Delta\zeta_{LGP} = +10\%$) and should be derived from viscometer measurements.

The current investigations only dealt with a moderate, low-loss gear geometry. In order to ensure general validity, a variation of the macro and micro gear geometry should be investigated and compared to mesh-averaged or contact-averaged methods.

Author contributions

Felix Farrenkopf: conceptualization, data curation, formal analysis, investigation, methodology, software, validation, visualization, writing—original draft, review, and editing; Thomas Lohner conceptualization, formal analysis, funding acquisition, supervision, writing—review & editing; Karsten Stahl funding acquisition, project administration, resources, writing—review & editing.

Declaration of competing interest

The authors have no competing interests to declare that are relevant to the content of this article.

References

[1] Bobach L, Bartel D, Beilicke R, Mayer J, Michaelis K, Stahl K, Bachmann S, Schnagl J, Ziegele H. Reduction in EHL friction by a DLC coating. *Tribol Lett* **60**(1): 17 (2015)

[2] Hinterstoißer M, Sedlmair M, Lohner T, Stahl K. Minimizing load-dependent gear losses. *Tribologie + Schmierungstechnik* **66**(3): 15–25 (2019)

[3] Marian M, Almqvist A, Rosenkranz A, Fillon M. Numerical micro-texture optimization for lubricated contacts: A critical discussion. *Friction* **10**(11): 1772–1809 (2022)

[4] Yilmaz M, Mirza M, Lohner T, Stahl K. Superlubricity in EHL contacts with water-containing gear fluids. *Lubricants* **7**(5): 46 (2019)

[5] ISO/TR 14179-2. *Gears-Thermal Capacity—Part 2: Thermal Load-Carrying Capacity*. Geneva (Switzerland): International Organisation for Standardisation, 2007.

[6] Ohlendorf H. Power loss andheating of spur gears. Dissertation. Munich (Germany): Technical University of Munich, 1958. (in German)

[7] Michaelis K. The integral temperature for evaluating the scuffing load capacity of spur gears. Munich (Germany): Technical University of Munich, 1987. (in German)

[8] Schlenk L. Investigations on the scuffing load capacity of large-sized gears. Dissertation. Munich (Germany): Technical University of Munich, 1995. (in German)

[9] Doleschel A. Efficiency calculation of gear drives depending on the lubricant. Dissertation. Munich (Germany): Technical University of Munich, 2003. (in German)

[10] Wimmer A. Load-dependent power loss of spur gears. Dissertation. Munich (Germany): Technical University of Munich, 2006. (in German)

[11] Benedict G H, Kelley B W. Instantaneous coefficients of gear tooth friction. *ASLE Trans* **4**(1): 59–70 (1961)

[12] Xu H, Kahraman A, Anderson N E, Maddock D G. Prediction of

mechanical efficiency of parallel-axis gear pairs. *J Mech Design* **129**(1): 58–68 (2007)
[13] Quiban R, Grenet De Bechillon N, Touret T, Navet P, Diab Y, Cavoret J, Ville F, Changenet C. On the interest of a semi-empirical model for the tooth friction coefficient in gear transmissions. *P I Mech Eng J-J Eng* **235**(12): 2654–2663 (2021)
[14] Arana A, Larrañaga J, Ulacia I. Partial EHL friction coefficient model to predict power losses in cylindrical gears. *P I Mech Eng J-J Eng* **233** (2): 303–316 (2019)
[15] Mayer J. Influence of surface and lubricant on friction in EHL contact. Dissertation. Munich (Germany): Technical University of Munich, 2013. (in German)
[16] Matsumoto S, Morikawa K. The new estimation formula of coefficient of friction in rolling-sliding contact surface under mixed lubrication condition for the power loss reduction of power transmission gears. In: Proceedings of the International Gear Conference, Lyon, France, 2014: 1078–1088.
[17] Grubin A. *Investigation of the Contact of Machine Components*. Moscow (Russia): Central Scientific Research Institute for Technology and Mechanical Engineering, 1949.
[18] Dowson D, Higginson G R. *Elasto-hydrodynamic Lubrication. International Series on Materials Science and Technology*. Oxford (UK): Pergamon Press, 1977.
[19] Hamrock B J, Dowson D. Isothermal elastohydrodynamic lubrication of point contacts: Part III: Fully flooded results. *J Lubr Technol* **99**(2): 264–275 (1977)
[20] Wang Y, Li H, Tong J, Yang P. Transient thermoelastohydrodynamic lubrication analysis of an involute spur gear. *Tribol Int* **37**(10): 773–782 (2004).
[21] Larsson R. Transient non-Newtonian elastohydrodynamic lubrication analysis of an involute spur gear. *Wear* **207**(1–2): 67–73 (1997)
[22] Mihailidis A, Panagiotidis K. Transient thermo-elastohydrodynamic lubrication of gear teeth. *Lubr Sci* **15**(4): 295–310 (2003)
[23] Ziegltrum A, Lohner T, Stahl K. TEHL simulation on the influence of lubricants on load-dependent gear losses. *Tribol Int* **113**: 252–261 (2017)
[24] Lohner T. Calculation of TEHL contacts and run-in behaviour of gears. Dissertation. Munich (Germany): Technical University of Munich, 2016. (in German)
[25] Beilicke R, Bobach L, Bartel D. Transient thermal elastohydrodynamic simulation of a DLC coated helical gear pair considering limiting shear stress behavior of the lubricant. *Tribol Int* **97**: 136–150 (2016)
[26] Bobach L, Beilicke R, Bartel D, Deters L. Thermal elastohydrodynamic simulation of involute spur gears incorporating mixed friction. *Tribol Int* **48**: 191–206 (2012)
[27] Farrenkopf F, Schwarz A, Lohner T, Stahl K. Analysis of a low-loss gear geometry using a thermal elastohydrodynamic simulation including mixed lubrication. *Lubricants* **10**(9): 200 (2022)
[28] Hinterstoißer M. On optimization of the efficiency of cylindrical gears. Dissertation. Munich (Germany): Technical University of Munich, 2014. (in German)
[29] Bartel D. *Simulation of Tribological Systems*. Wiesbaden (Germany): Vieweg + Teubner, 2010.
[30] Weinberger U, Otto M K, Stahl K. Closed-form calculation of lead flank modification proposal for spur and helical gear stages. *J Mech Design* **142**: 31106 (2020)
[31] DIN ISO 21771. Gears—Cylindrical involute gears and gear pairs—Concepts and geometry. German Institute for Standardization, 2014.
[32] Paschold C, Sedlmair M, Lohner T, Stahl K. Calculating component temperatures in gearboxes for transient operation conditions. *Forsch Ingenieurwes* **86**: 521–534 (2022).
[33] Habchi W. *Finite Element Modeling of Elastohydrodynamic Lubrication Problems*. Newark (USA): John Wiley & Sons Incorporated, 2018.
[34] Patir N, Cheng H S. Effect of surface roughness on the central film thickness in EHD contacts. In: Proceedings of the 5th Leeds-Lyon Symposium on Tribology, Leeds, UK, 1978.
[35] Patir N, Cheng H S. An average flow model for determining effects of three-dimensional roughness on partial hydrodynamic lubrication. *J Lubr Technol* **100**: 12–17 (1978)
[36] Bobach L, Beilicke R, Bartel D. Transient thermal elastohydrodynamic simulation of a spiral bevel gear pair with an octoidal tooth profile under mixed friction conditions. *Tribol Int* **143**: 106020 (2020)
[37] Venner C H, Lubrecht A A. *Multilevel Methods in Lubrication*. New York (USA): Elsevier, 2000.
[38] Roelands C J A. Correlational aspects of the viscosity-temperature-pressure relationship of lubricating oils. Ph. D. Thesis. Delft (the Netherlands): Technical University of Delft, 1966.
[39] Vogel H D. The temperature dependence law of the viscosity of liquids. *Phys Z* **22**: 645 (1921) (in German)
[40] Fulcher G S. Analysis of recent measurements of the viscosity of glasses. *J Am Ceram Soc* **75**(5): 1043–1055 (1992)
[41] Tammann G, Hesse W. The dependency of viscosity on the temperature of supercooled liquids. *Z Anorg Allg Chem* **156**(1): 245–257 (1926) (in German)
[42] Bode B. Model for describing the rheological behaviour of liquids under high pressure. *Tribol Schmier* **36**: 182–189 (1989)
[43] Larsson R, Andersson O Lubricant thermal conductivity and heat capacity under high pressure. *P I Mech Eng J-J Eng* **214**(4): 337–342 (2000)
[44] Eyring H. Viscosity, plasticity, and diffusion as examples of absolute reaction rates. *J Chem Phys* **4**(4): 283–291 (1936)
[45] Neupert T, Bartel D. Evaluation of various shear-thinning models for squalane using traction measurements, TEHD and NEMD simulations. *Lubricants* **11**(4): 178 (2023)
[46] Neupert T, Bartel D. Reply to Bair, S. Comment on "Neupert, T.; Bartel, D. Evaluation of various shear-thinning models for squalane using traction measurements, TEHD and NEMD simulations. *Lubricants* 2023, 11, 178". *Lubricants* 11(9): 394 (2023)
[47] Bair, S. Comment on "Neupert, T.; Bartel, D. Evaluation of Various Shear-Thinning Models for Squalane Using Traction Measurements, TEHD and NEMD Simulations. *Lubricants* 2023, 11, 178". *Lubricants* 11(9): 393 (2023)
[48] Lohner T, Ziegltrum A, Stemplinger J P, Stahl K. Engineering Software Solution for Thermal Elastohydrodynamic Lubrication Using Multiphysics Software. *Advances in Tribology* **1**: 6507203 (2016)
[49] Coulomb C A Théorie des machines simples (Nouv. éd). 1821.
[50] Schweigert D, Weinberger U, Otto M, Stahl K. Advanced method of including housing stiffness into calculation of gear systems. *Forsch Ingenieurwes* **86**: 241–248 (2022).
[51] Yilmaz M, Önüt A, Lohner T, Stahl K. Gear and bearing power losses: From dip to minimum quantity lubrication. *Ind Lubr Tribol* **74**(9): 985–994 (2022)
[52] Höhn B R, Michaelis K, Otto H P. Minimised gear lubrication by a minimum oil/air flow rate. *Wear* **266**(3–4): 461–467 (2009)
[53] Ziegltrum A, Emrich S, Lohner T, Michaelis K, Brodyanski A, Merz R, Kopnarski M, Hoehn B R, Stahl K. Influence of tribofilms on failures and friction of gears with particular focus on running-in. *Ind Lubr Tribol* **71**(8): 1017–1026 (2019)

Felix Farrenkopf got his master degree in mechanical engineering at Technical University of Munich, Germany. Since 2019, he has been working as research associate at Gear Research Center (FZG) in the department EHL-Tribological-Contact and Efficiency, Germany. He is specialized in the fields of gear tribology with focus on simulation of elastohydrodynamically lubricated and dry rolling-sliding contacts.

Thomas Lohner is a postdoctoral researcher and the head of the EHL-Tribological-Contact and Efficiency department at the Gear Research Center (FZG) of the Technical University of Munich (TUM), Germany. His research focuses on the tribology of gears and the efficiency and heat balance of geared transmissions, using of multi-scale modeling and experimental methods. He deals with gearbox fluid and heat flow, elastohydrodynamics of gear contacts, superlubricity with aqueous lubricants, oil-lubricated thermoplastics, minimum quantity lubrication, tribological coatings, loss of lubrication and superefficiency.

Karsten Stahl is a full time professor at the Gear Research Center (FZG) at the Technical University of Munich, Germany, since 2011. His research topics include the development of methods and tools of reliable determination of fatigue life, efficiency, and vibration characteristics of gears and transmission elements.